

Experimental demonstration of non-local magic in a superconducting quantum processor

Halima Giovanna Ahmad^{1†}, Gianluca Esposito^{2,3†}, Viviana Stasino¹, Jovan Odavić^{1,3}, Carlo Cosenza¹, Alessandro Sarno¹, Pasquale Mastrovito¹, Michele Viscardi^{1,3}, Stefano Cusumano^{1,3}, Francesco Tafuri^{1*}, Davide Massarotti⁴, Alioscia Hamma^{1,2,3*}

¹Dipartimento di Fisica “Ettore Pancini”, Università degli Studi di Napoli “Federico II”, Complesso Universitario di Monte Sant’Angelo, Via Cinthia, 21, Napoli, 80126, Italy.

²Mathematical and Physical Sciences for Advanced Material and Technologies, Scuola Superiore Meridionale, Via Mezzocannone, 4, Napoli, 80134, Italy.

³Istituto Nazionale di Fisica Nucleare (INFN), Sezione di Napoli, Complesso Universitario di Monte Sant’Angelo, Via Cinthia, 21, Napoli, 80126, Italy.

⁴Dipartimento di Ingegneria Elettrica e delle Tecnologie per l’Informazione, Via Claudio, Napoli, 80125, Italy.

*Corresponding author(s). E-mail(s): francesco.tafuri@unina.it; alioscia.hamma@unina.it;

†These authors contributed equally to this work.

Magic is a non-classical resource whose efficient manipulation is fundamental to advancing efficient and scalable fault-tolerant quantum computing. Quantum advantage is possible only if both magic and entanglement are present. Of particular interest is non-local magic - the fraction of the resource that cannot be distilled (or erased) by local unitary operations - which is a necessary feature for quantum complex behavior. We perform the first experimental demonstration of non-local magic in a superconducting Quantum Processing Unit (QPU). Direct access to the QPU device enables us to identify and characterize the dominant noise mechanisms intrinsic to the quantum hardware. We observe excellent agreement between theory and experiment without the need for any free parameter in the noise modeling of our system and shows the experimental capability of harnessing both local and non-local magic resources separately, thereby offering a promising path towards more reliable pre-fault-tolerant quantum devices and to advance hardware-aware research in quantum information in the near term. Finally, the methods and tools developed in this work are conducive to the experimental realization of efficient purity estimation (featuring exponential speedup) and the decoding of Hawking radiation from a toy-model of a Black Hole.

An essential objective in quantum information science is to identify the physical resources that lead to quantum computational speedups over classical algorithms [11–15]. Entanglement is necessary for universal fault-tolerant quantum computation, though not sufficient for quantum advantage. A common paradigm for fault-tolerant operations uses the stabilizer formalism [1, 16]. In this framework, the additional resources needed for quantum advantage are non-stabilizer states, namely those resources that go beyond Clifford operations, also colloquially known as *magic* [2, 3, 17]. A system that only uses stabilizer operations may have access to extensive entanglement (and no magic), while exclusively using local operations allows for generation of extensive magic (but no entanglement). Notably, in both cases these systems can be efficiently simulated on a classical computer. For this reason, the onset of both quantum complex behavior and quantum advantage resides in the interplay between the two resources [6–8, 18–22].

So-called *non-local magic* [23] is a recent resource introduced to capture the interplay between entanglement and magic. It quantifies the fraction of non-stabilizer resources that cannot be removed by local unitary operations and operationally represents the amount of magic that cannot be distilled using local operations. Even in the NISQ [24] era, local and non-local magic are both believed to be

crucial for universal quantum computation [4]: in quantum algorithms that rely on the preparation of complex quantum states exhibiting non-local magic [25], or in magic state distillation processes in fault-tolerant quantum computing, where stabilizer codes are used to purify non-stabilizer states and achieve fault-tolerant non-Clifford operations [26, 27]. Notably, non-local magic can also be a hindrance to some genuine quantum behavior. For instance, if a state only contains non-local magic, then no Bell inequality violations can occur [28]. Non-local magic plays a role in the flourishing field of Anti-de Sitter/Conformal Field Theory (AdS/CFT) correspondence, representing the holographic counterpart of gravitational back-reaction [23]. This connection thus provides an additional intriguing link between quantum advantage, error-correcting codes and holography [29].

In this paper, we give the first experimental demonstration and measurement of non-local magic on a superconducting QPU shown in Fig. 1. We utilize Stabilizer (Rényi) Entropy (SRE) - the unique computable measure of magic for pure states - which is experimentally measurable [30–32] via Randomized Measurement toolbox [33]. Our main result is that non-local magic is measurable in real quantum devices. We measure it using two different methods in three classes of states: i) those that have mostly

local magic, ii) those with both local and non-local magic, and iii) those only possessing non-local magic. The first method involves measuring residual magic after an optimal local erasure protocol given the preparation and noise, and the second, more direct approach hinges on measuring the Schmidt coefficients via reduced density matrix (RDM) [34]. Across the three classes of states, the two methods yield results consistent both with the theoretical predictions and with each other.

In the NISQ era of quantum devices it becomes of paramount importance to investigate the relationship between experimentally measured magic on real devices and noise sources, as well as the characteristic physical parameters of the hardware itself. Our experimental investigation opens new avenues for studying the impact of noise sources on quantum hardware. We find that the greater source of error is given by readout errors, which are responsible for injecting local magic. Moreover, noise and decoherence will generally reduce state purity, hence one needs to maintain the state at a very high purity. Here, we show that non-local noise can be modeled as a depolarizing Controlled-Z (CZ) channel and can be taken into account in the quantum state preparation. This noise mainly affects the optimal local magic erasure protocol, while being gentle on the overall purity. In comparison, readout noise is more impactful, but it can be tackled by error mitigation techniques [35, 36].

Our approach to readout-noise mitigation reinforces the idea that both local and non-local magic measurement can be used to benchmark and calibrate quantum devices beyond state-of-the-art protocols, e.g. Randomized Benchmarking (RB), which extensively rely on Clifford gates to benchmark gate fidelities [37–39]. We complement recent proposals, which include the use of non-Clifford gates to benchmark gate fidelity [40, 41], though lacking information about the ability to generate and eventually manipulate magic for quantum advantage. Therefore, our framework may help tackling current challenges in hardware-aware quantum algorithms in the NISQ era, advancing gate calibration and optimization, as well as benchmarking computational resources for quantum advantage in an accessible way.

Local and non-local stabilizer entropy

Stabilizer entropy characterizes the extent to which a quantum state spreads over the Pauli operator basis, serving as a measure of its departure from stabilizer states [30]. The α SRE is defined as

$$M_\alpha(\psi) = \frac{1}{1-\alpha} \log_2 \left(\frac{1}{d} \sum_{P \in \mathcal{P}_N} |\text{Tr}(P\psi)|^{2\alpha} \right), \quad (1)$$

where $\psi = |\psi\rangle\langle\psi|$ is the density matrix of the N -qubit pure state $|\psi\rangle$ of dimension $d = 2^N$. The set \mathcal{P}_N represents the N -qubit Pauli strings composed from the identity and Pauli operators $\{\mathbb{1}, X, Y, Z\}$. For pure states, SRE with $\alpha \geq 2$ constitutes a proper magic monotone in the context of magic-state resource theory [30, 31]. For mixed states, this quantity can be extended by subtracting the 2-Rényi

entropy, that is, $-\log_2(\mathcal{P}(\psi))$ where $\mathcal{P}(\psi) = \text{Tr}(\psi^2)$ is the purity of ψ .

The interplay between entanglement and magic is non-trivial: for example, factorized states cannot have maximum amount of magic even though the most commonly used magic-injecting gate, the T gate, is a single-qubit gate. This means that entanglement is necessary to reach higher values of magic, and the value of magic obtainable in a state is influenced by its entanglement [18]. This simple fact suggests that there is an inherently *non-local* part of magic that arises by using both non-Clifford and entangling gates together. By construction, such non-local magic cannot be extracted, or erased from a state by means of local unitaries.

Non-local magic is defined as follows [23]: given $\mathcal{H} = \mathcal{H}_A \otimes \mathcal{H}_B$, then $M_2^{\text{NL}}(|\psi\rangle) = \min_{U_A, U_B} M_2(U_A \otimes U_B |\psi\rangle)$, or in other words, the minimal amount of magic contained in a bipartite state upon optimization in all local bases. Conversely, *local* magic of a state is defined as the difference between the total magic and the non-local one $M_2^{\text{L}}(|\psi\rangle) = M_2(|\psi\rangle) - M_2^{\text{NL}}(|\psi\rangle)$ and corresponds to the amount of magic that *can* be removed from a state with local gates. Notice that non-local magic is not simply magic in entangled states: there are entangled states that only host local magic, as in any state of the form $(U_A \otimes U_B)C|0\rangle$ where $C|0\rangle$ is an entangled stabilizer state. Remarkably, maximally entangled states only possess local magic.

Despite being the result of an optimization procedure, non-local magic is analytically computable for pure two-qubit states [5] and is tied to the Schmidt decomposition of the state. We denote the class of states achieving $M^{\text{NL}}(|\psi_\lambda\rangle) = M(|\psi_\lambda\rangle)$ as *non-local magic states*. Moreover, for two qubit states, non-local magic is a function of the purity of the reduced density matrix (RDM) $\psi_A := \text{Tr}_B |\psi\rangle\langle\psi|$ (see *Methods* for details):

$$M^{\text{NL}}(|\psi\rangle) = -\log_2 (4\mathcal{P}(\psi_A)^2 - 6\mathcal{P}(\psi_A) + 3). \quad (2)$$

This effectively amounts to measuring non-local magic from the anti-flatness of the entanglement spectrum, as proposed in [23]. Thus, by measuring RDM purity, we get a direct measurement of a state's non-local magic to test the local optimal erasure protocol against. In this work we focus on the experimental realization of a minimal setting involving two qubits, and investigate representative examples of Local Magic (LM), Local + Non-Local Magic (M) and Non-Local Magic (NLM) states. In the following, we measure non-local magic both from the local optimal erasure protocol via local unitaries (obtained numerically and then implemented on quantum hardware) and from subsystem purity measurements. Taken together, these two approaches provide a bona-fide experimental confirmation of non-local magic.

Despite the nascent importance of non-local magic in understanding quantum physics phenomena [5, 19, 23], its role in quantum algorithms and broader quantum information processing tasks is yet to be fully understood. As a preliminary step in this direction, we prove a lemma, found in *Supplemental Information*, which establishes that the local magic is the maximum amount of magic that

can be distilled from a two-qubit state to a third ancillary state without disrupting the entanglement of the two initial qubits. Such a scenario can be relevant in realistic quantum computing protocols, as the possibility of implementing multi-qubit gates can be limited by the physical connectivity of the quantum hardware.

The device

The superconducting Quantum Processing Unit (sQPU) used in this work is a Contralto-D from Quantware (Fig. 1 (a)), composed of 21 flux-tunable transmons and 4 fixed-frequency transmon qubits (in yellow). The fixed-frequency qubits are specifically designed for coherence times benchmarking, i. e. they lack drive lines to minimize radiative interaction with the environment, are isolated and not affected by flux noise. The sQPU is thermally and mechanically anchored at the coldest stage of a BlueforsXLD1000SL (the mixing chamber, MXC), and is enclosed by two magnetic shields. At room temperature, the system uses Qblox electronics, which is comprised of two main parts: Clusters (equipped with RF modules to implement drive, readout, and two-qubit gates) and a low-noise SPI rack for setting static DC flux. The full description of the setup is reported in *Supplemental Information*.

The 21-qubits matrix has rectangular 2D connectivity, where high-frequency bus resonators (in grey) are used to couple neighboring qubits [42]. Qubits are designed to fall in three frequency bandwidths: high-frequency qubits (in red) have frequencies of the order of 6 GHz, intermediate frequency qubits (in blue) have frequencies of the order of 5 GHz, low frequency qubits (in green) lie in a frequency range of the order of 4 GHz. Each qubit is equipped with a dedicated superconducting readout resonator, equally distributed over 4 readout feedlines in a notch-type geometry (highlighted with different colors for clarity), hence guaranteeing multiplexed readout. Dedicated drive and flux lines are used to implement X, Y, Z single-qubit and two-qubit gates, respectively [43]. In fact, flux-lines are used to implement the native two-qubit gate of the processor, the Controlled-Z (CZ) gate, using magnetic Sudden-Net-Zero (SNZ) flux pulsed signals [44], combined with low $1/f$ -noise static flux fields through bias-tees at room-temperature. Flux lines also allow for parking qubits at specific working points by using a static magnetic flux.

In this work, we focus on qubits D3 and C4 (intermediate and low frequency qubits), operated at their flux sweet spots (Fig. 1 (b)). Additionally, the neighboring qubit A6 has been placed at its sweet spot (at least 1 GHz detuned from the interested qubits), whereas the remaining qubits of the matrix are operated at their anti-sweet spot (in black). This allows us to operate in a quasi-ideal 2-qubit register and avoid frequency crowding. Notably, flux-tunable transmons in the processor are designed to be symmetric [45].

QPU's non-local magic measurements

To overcome the exponential cost of direct measurement of SRE with qubit number, we use a more scalable protocol, namely Randomized Clifford Measurements (RCM)[32]. Anticipating purity-impacting noise in our device, we use

the mixed-state extension of SRE. Thus, our experimental approach consists of two main steps: i) preparation of an N -qubit state ψ ; ii) implementation of the RCM protocol to evaluate purity \mathcal{P} and stabilizer purity \mathcal{W} of the prepared state ψ . These two independent quantities enable estimation of SRE according to

$$M_2(|\psi\rangle) = -\log_2 \mathcal{W} + \log_2 \mathcal{P} - \log_2 d, \quad (3)$$

where $\mathcal{P} = d \sum_{\mathbf{s}} (-2)^{-\|\mathbf{s}\|_2} \mathbb{E}_C [P(\mathbf{s}_1|C)P(\mathbf{s}_2|C)]$, and $\mathcal{W} = -\sum_{\mathbf{s}} (-2)^{-\|\mathbf{s}\|_4} \mathbb{E}_C [P(\mathbf{s}_1|C)P(\mathbf{s}_2|C)P(\mathbf{s}_3|C)P(\mathbf{s}_4|C)]$. Here, \mathbf{s}_i denote computational basis strings, and $\|\cdot\|$ refers to their corresponding Hamming weight. The expectation value \mathbb{E}_C indicates averaging over different random choices of single-qubit Clifford gates C . To ensure statistical reliability, a sufficiently large number of samples must be considered, as discussed in Ref. [32].

After a thorough characterization and benchmarking of the qubits, including measurements of readout and gate fidelities, coherence times, and crosstalk effects, we performed measurements of the SRE for the quantum states summarized in Fig. 1 (c-f). The corresponding experimental results are presented in Extended Data Table 1, which reports the measured fidelities, coherence, and crosstalk parameters. These data provide direct insight into how the relevant sources of error affect the estimation of magic in our device.

We begin by considering single-qubit states prepared on both the D3 and C4 qubits. Specifically, we examine the computational basis state $|0\rangle$ and the superposition states $|+\rangle$ and $|-\rangle$, obtained by initializing the qubit in either $|0\rangle$ or $|1\rangle$ and subsequently applying a Hadamard gate, as illustrated in Fig. 1 (c) and (d). In these experiments, we expect vanishing magic. By contrast, when a T gate is introduced, the experimentally measured magic increases and approaches the theoretical value of $\log_2(4/3) \approx 0.41$. Next, we measure magic for two-qubit quantum states according to the circuit depicted in Fig. 1 (e). At this stage, we choose not to implement any entangling gate between the two qubits. Since magic is additive, experimental results demonstrate that RCM can obtain experimental magic values consistent with the sum of the values measured in the isolated case, both with and without the injection of non-Clifford gates. Additivity is consistent with the fairly low impact of microwave and ZZ crosstalk [46, 47].

Finally, we measure magic for a Bell state, thus including more complexity and hardware noise sources in the experiment (see Fig. 1 (f)). From Extended Data Table 1 one notices: i) readout fidelities are lower in the case of two-qubit states; ii) interleaved RB fidelities for the native two-qubit gate CZ is considerably lower than single-qubit gate RB fidelities, either measured in the isolated (a) and coupled scheme (b), thus implicitly including any microwave or ZZ-crosstalk. This explains the presence of non-zero experimental magic in those cases where one does not expect any.

We employ a classical post-processing error mitigation scheme to counteract the effect of readout errors. This scheme directly uses information from different benchmarking tools to single out sources of crosstalk, thanks to direct experimental control of the chip. In particular, our scheme relies on the knowledge of the readout calibration matrix

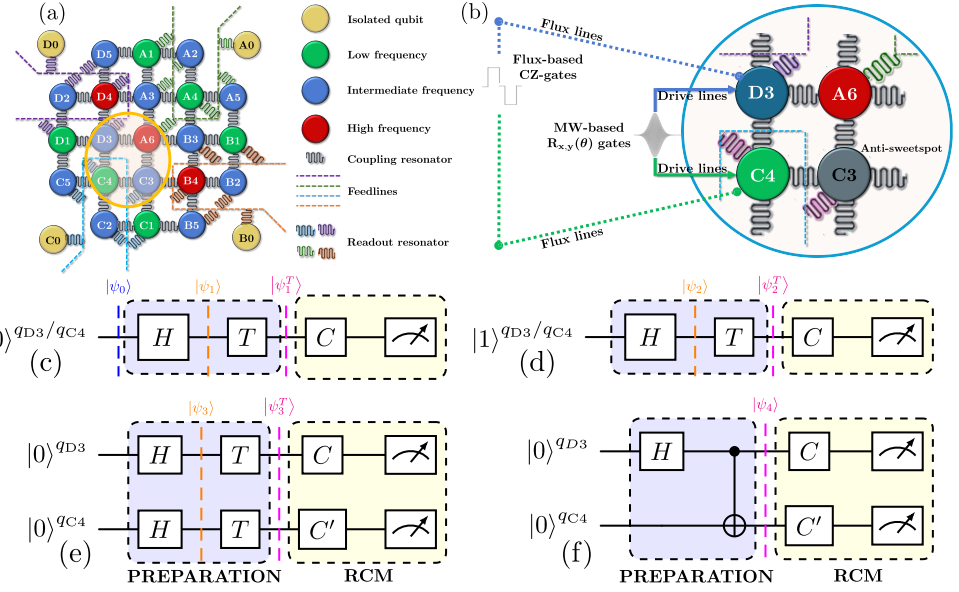


Fig. 1: Superconducting Quantum Processing Unit and Benchmarking Circuits. (a, b) Processor schematics. In (a), overview of the superconducting quantum processor. In (b), focus on the investigated pair (D3–C4), coupled with a high-frequency qubit (A6) parked at its sweet spot and a low-frequency qubit (C3) at the anti-sweet spot (in black). (c–f) Benchmarking circuits. The colored quantum states correspond to the injection (purple) and non-injection (orange) of non-Clifford T gates. The measurement block represents the RCM protocol.

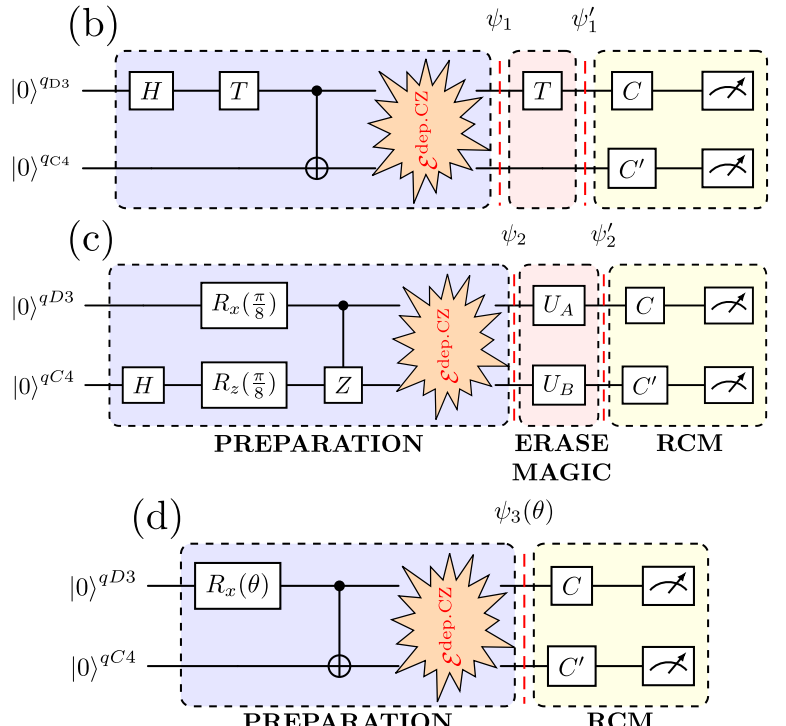
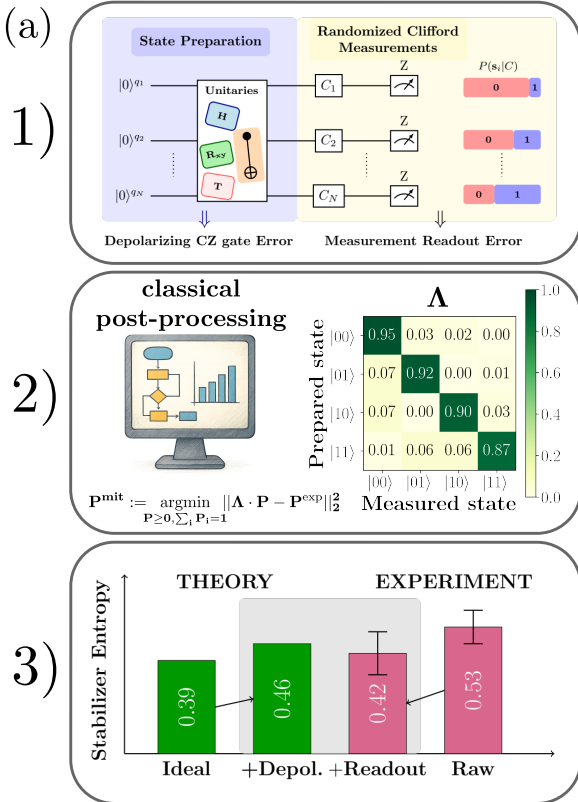


Fig. 2: Experimental approach and investigated circuits. (a) Experimental approach for magic measurement and error mitigation. The studies of LM, M, and NLM quantum states involve: (1) preparing target states and performing standard benchmarking protocols to extract CZ gate fidelity and readout calibration matrix Λ , (2) using Λ in classical post-processing to obtain error-mitigated probabilities $P(\mathbf{s}_i|C)$, and (3) adjusting theoretical predictions for stabilizer entropy and purity given the observed CZ depolarizing error in case of the M state ψ_2 . (b–d) Investigated circuits. The first two experiments comprise preparation and erasure protocols, while the third involves only non-local magic, confirmed by RDM-purity-inferred data (see Fig. 3(b)). In all panels, the depolarizing CZ error $\mathcal{E}_p^{\text{dep. CZ}}$ is accounted for at the theoretical-prediction level.

(see *Methods*). This makes the error mitigation procedure

“parameter free”, as it does not require any fitting parameter across a vast set of experiments, as done in other works, such as Ref. [32].

State	Circuit	State	Th. Purity	Exp. Purity	Th. Magic	Exp. Magic	NL-Magic (from RDM purity)
Local Magic (LM)	Fig. 2(b)	ψ_1	0.94	0.90 ± 0.04	0.48	0.38 ± 0.09	0.0888 ± 0.0004
		ψ'_1	0.94	0.93 ± 0.05	0.08	0.1 ± 0.1	
Non-Local (M)	Fig. 2(c)	ψ_2	0.94	0.94 ± 0.04	0.46	0.42 ± 0.09	0.19 ± 0.07
		ψ'_2	0.94	1.00 ± 0.05	0.27	0.3 ± 0.1	

Table 1: Comparison of purity and magic. Obtained values for states ψ_i (before) and ψ'_i (after) local magic erasure for $i = \{1, 2\}$, as well as the value of non-local magic obtained from subsystem purity by tracing out qC4 qubit. The theoretical predictions for purity and magic are calculated by considering the CZ depolarizing error and compared with the experimental results after readout error mitigation. Details on the errors are reported in *Methods*.

In our hardware, CNOT is decomposed in terms of a combination of single-qubit Hadamard gates and the CZ gate. Motivated by the relatively larger CZ errors on the measured purity and stabilizer entropy, we account for its influence on the theoretical prediction side by modeling the effects as a depolarizing channel (see *Methods*), with a depolarization strength directly based on the IRB CZ fidelity. Our approach allowing for a consistent comparison between theoretical expectations and the experimental outcomes, is summarized Fig. 2 (a).

Next, we focus on three specific quantum circuits preparing LM, M and NLM states, shown in Fig. 2 (b-d). Accounting for CZ depolarizing error at the theory level and post-processing of readout error mitigation in concert has been instrumental for the experimental detection of non-local magic.

Local Magic (LM) state. We first consider a circuit that only hosts local magic injected by a T gate, despite the state being maximally entangled (see Fig. 2(b)). The preparation circuit output reads $\psi_1 = \mathcal{E}_p^{\text{dep.CZ}}[2^{-1/2}(|00\rangle + e^{i\frac{\pi}{4}}|11\rangle)]$. Evaluation of stabilizer entropy for this state yields $M_2(\psi_1) \sim 0.48$. One removes or erase local magic in the state by applying another T gate on the same qubit, yielding $M_2(\psi'_1) \sim 0.1$. This constitutes a minimal example where we are able to (almost) completely remove magic with a local gate. We observe consistency between theoretical expectations and experimental results for both purity and stabilizer entropy within the statistical error associated with the RCM, together with the results obtained by the measurement of RDM purity, as seen in Table 1.

Local+Non-Local Magic (M) state. We measure the response of the quantum circuit in Fig. 2(c) for which the output state has both local and non-local magic. The output state of the preparation circuit reads $\psi_2 = \mathcal{E}_p^{\text{dep.CZ}}[2^{-3/2}(c_+ (|00\rangle + e^{i\frac{\pi}{8}}|10\rangle) - i c_- (|01\rangle + e^{i\frac{\pi}{8}}|11\rangle)]$, with $c_{\pm} = (2 \pm (2 + \sqrt{2})^{\frac{1}{2}})^{\frac{1}{2}}$, and stabilizer entropy is $M_2(\psi_2) \sim 0.46$. Since this state has both local and non-local magic, one expects to be able to partially erase magic using single-qubit gates. Numerical optimizations yield the following local magic-erasing unitaries: $U_A = R_z(\alpha)R_y(\beta)R_z(\gamma)$ and $U_B = R_z(\delta)R_y(\eta)R_z(\phi)$, with the rotation angles $\alpha = \beta = \gamma = \delta = \eta = 0$ and $\phi = 67.61^\circ$. Experimental data strongly validates theoretical predictions, as summarized in Tab. 1.

Non-Local Magic (NLM) states. We consider a two-qubit state of the form $\psi_3(p, \theta) = \mathcal{E}_p^{\text{dep.CZ}}[\cos(\theta/2)|00\rangle - i \sin(\theta/2)|11\rangle]$, realized by the quantum circuit in Fig. 2(d). This state only hosts non-local magic, and including the depolarizing CZ noise channel

we obtain the following closed-form expression for the stabilizer entropy $M_2(\psi_3(p, \theta)) = -\log_2 [4((p-1)^4 \cos(4\theta) + 5(p-2)p((p-2)p+2) + 7)] + \log_2(3(p-2)p+4) + 3$. A systematic investigation of the stabilizer entropy as a

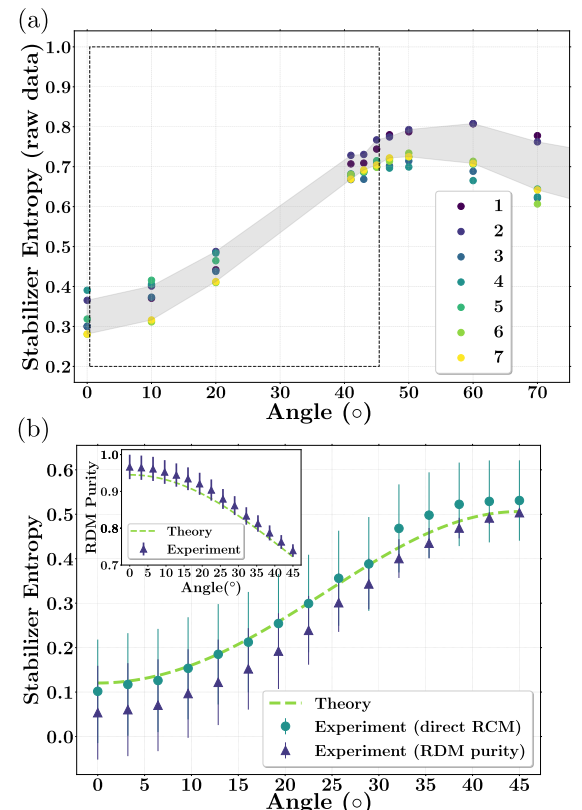


Fig. 3: NLM state experiment results (Fig. 2, panel (d)). In (a), experimental raw data repeated over 7 runs for the NLM quantum state. The shadowed gray area highlights fluctuations between different experiments. In (b), focus on experimental readout-error-mitigated data with a smaller angle interval (dashed box in panel (a)) as well as the values of non-local magic obtained by RDM purity compared to the theoretical line of the stabilizer entropy and RDM purity (inset) with CZ depolarizing errors taken into account.

function of θ is reported in Fig. 3. In panel (a), the raw experimental data for stabilizer entropy is shown for multiple independent runs. We recognize that for $\theta = \pi/2$ the resulting state is the Bell state $|\Psi_4\rangle$ in Extended Data Table 1. Theoretically, this state is expected to have vanishing stabilizer entropy, while for $\theta = \pi/4$, we anticipate maximum non-local magic. However, we measure a strong asymmetry between rotations below and above $\pi/4$, with

considerable fluctuations, much larger than the statistical error bars for the respective runs. This asymmetry cannot be explained by readout and CZ depolarizing errors. For $\theta > \pi/4$, the nature of the error is yet to be addressed thoroughly, but it is beyond the scope of our work. At this stage, we consider the data for $\theta \leq \pi/4$ and observe excellent agreement between experimental data and theoretical predictions, as shown in Fig. 3(b).

Discussions and Conclusions

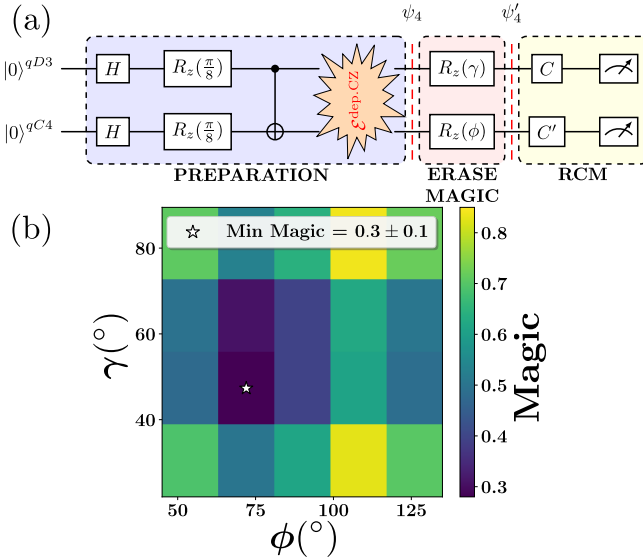


Fig. 4: Quantum circuit for Local+Non-local magic quantum state with CNOT gate. Panel (a): circuit representation of the sweeping protocol for empirically estimating the optimal magic erasure angles. The minimum amount of theoretically obtainable magic using R_z rotations is 0.29 with $(\gamma, \phi) = (67.5^\circ, 90^\circ)$. Panel (b): results, with the star marking the values of the angles for which the state has minimal magic. The sweeping angles method reaches the same minimum value as theoretically predicted, although for different angles than anticipated.

Genuine quantum advantage only arises with coexistence between non-stabilizerness and entanglement, with non-local magic capturing such an interplay [25, 48], and here we provided its first experimental measurement on a QPU.

Currently there is no unique way to precisely benchmark the performance of QPUs across the various quantum circuit designs and error-mitigation schemes, hence the link between magic manipulation of NISQ devices and the physical characteristics of hardware, as well as its noise sources, is a pressing challenge. The quantum processor used in this work, core of the first Italian Superconducting Quantum Computing Center (*Partenope*), fits all the criteria of the challenge, allowing a custom-tailored error mitigation approach directly based on the experimental performances of the device. This was key for the experimental demonstration of local magic erasure from a given state and non-local magic experimental observation using subsystem purity.

Our hardware-informed noise modeling correctly identifies measurement readout and CZ depolarizing noise

as main noise sources of the QPU. Readout errors are especially relevant for injecting local magic, whereas depolarizing noise keeps the non-local structure of magic intact. Despite these two channels not being the only noise sources in our devices, as magic measurements on the NLM experiment for $\theta > 45^\circ$ shows, we demonstrate that addressing the most impacting noise sources suffices to correctly characterize non-local features of magic. However, quantum devices are complex systems, and more sophisticated noise-mitigation techniques may become necessary to account for State Preparation and Measurement (SPAM) errors, that arise when increasing the number of gates in circuit preparation. Nonetheless, the ability to erase local magic does not depend on the full knowledge of the noise channels affecting the chip.

We present a proof-of-concept protocol showing it is possible to empirically identify optimal unitaries that erase local magic in situ, shown in Fig. 4. The protocol is partly informed by theory which identifies a restricted set where the optimal erasing unitaries lie. Then, by sweeping the rotation angles in the relevant interval we empirically isolate actual gates that erases local magic, the results of which are in Fig. 4 (b). The minimum local magic value closely matches the theoretical expectation for the investigated state, although the experimental angles are different than the predicted ones. This implies other noise sources affect the hardware beyond the theoretical model, and highlights the promise of heuristically determining the local magic-erasing unitaries.

In conclusion, the study of local and non-local magic resources cannot neglect the noisy nature of the hardware. Our work opens a rich playground to benchmark and calibrate quantum devices of different architectures beyond traditional gate fidelity protocols, and we envision these benchmarks can be extended to other quantum platforms as well. We also foresee the experimental accessibility of quantum systems where non-local magic plays a role: from violations of Bell's inequalities in NLM states [28], to the toy-modeling of black holes in a laboratory. The harnessing of non-local magic is preliminary to the experimental capability of moving magic around the system and cleansing subsystems from their local magic. With the ability to confidently manipulate a larger number of qubits, we anticipate the application of novel algorithms that demonstrate the capacity to decode the Hawking radiation from a black hole without previous knowledge of the initial state [10, 49, 50]. The kernel of these quantum algorithms has already inspired applications in more generic scenarios of quantum information processing, promising exponential advantage over state-of-the-art metrology protocols such as purity estimation [9]. We propose that with proper knowledge of magic manipulation abilities of one's quantum device, such algorithms can be implemented on real quantum hardware.

Methods

Non-local magic as a function of RDM purity

In this section, we derive the expression of non-local magic as a function of RDM purity, valid in the case of two-qubit states. Any pure two qubit state $|\psi\rangle$ can be written in the following way: $|\psi\rangle = \sqrt{\lambda}|\psi_1^A\rangle|\psi_1^B\rangle + \sqrt{1-\lambda}|\psi_2^A\rangle|\psi_2^B\rangle$, where $\{\lambda, 1-\lambda\}$ are called Schmidt coefficients and $\{|\psi_1^X\rangle, |\psi_2^X\rangle\}$ is the Schmidt basis of \mathcal{H}_X , with $X \in \{A, B\}$. Given this expression, the non-local magic of $|\psi\rangle$ is equal to

$$M^{\text{NL}}(|\psi\rangle) = -\log_2 (4(\lambda-1)\lambda(1-2\lambda)^2 + 1), \quad (4)$$

with states achieving $M^{\text{NL}}(|\psi_\lambda\rangle) = M(|\psi_\lambda\rangle)$ being of the form $|\psi_\lambda\rangle = \sqrt{\lambda}|00\rangle + \sqrt{1-\lambda}|11\rangle$, and $|00\rangle, |11\rangle$ being states of the computational basis, i.e. the eigenstates of the Z -Pauli matrix. Note that Eq. (4) reduces to the one derived in [5] when one parametrizes the Schmidt coefficients as $\{\cos(\theta/2), \sin(\theta/2)\}$, i.e.

$$M^{\text{NL}}(\theta) = \log_2 (8(7 + \cos(4\theta))^{-1}). \quad (5)$$

Since non-local magic depends exclusively on the Schmidt spectrum, in the unique case of two-qubit states one is able to measure the Schmidt coefficients by measuring a single quantity, e.g. subsystem purity. Starting from a pure state $|\psi\rangle$ in the Schmidt form, the purity of the RDM $\psi_A := \text{Tr}_B |\psi\rangle\langle\psi|$ is given by $\mathcal{P}(\psi_A) = \lambda^2 + (1-\lambda)^2$. Inverting this relationship and substituting it in Eq. (4), we get an explicit function of non-local magic on RDM purity:

$$M^{\text{NL}}(|\psi\rangle) = -\log_2 (4\mathcal{P}(\psi_A)^2 - 6\mathcal{P}(\psi_A) + 3). \quad (6)$$

This method of deriving M^{NL} remains valid also in the presence of noise, although the expression will be different than the one shown in Eq. (6). More specifically, the relationship between $\mathcal{P}(\psi_A)$ and λ will change according to the action of the specific noise channel, and will depend on the noise parameters $\vec{\mathbf{p}}_{\text{noise}}$ as well. Nevertheless, again inverting such relation and obtaining $\lambda(\mathcal{P}(\psi_A), \vec{\mathbf{p}}_{\text{noise}})$ and plugging it in Eq. (4) one obtains an expression of M^{NL} as a function of $\mathcal{P}(\psi_A)$ (and $\vec{\mathbf{p}}_{\text{noise}}$, that need to be determined experimentally).

Randomized Clifford Measurements experimental parameters and errors

The RCM protocol exploits the use of a randomized set of Clifford unitaries to estimate, by sample average, the purity and the stabilizer purity. The cardinality of the possible N -qubit Clifford unitaries (modulo global phase $U(1)$) [51] that are randomly picked from the Clifford group reads as

$$|\overline{C_N}| = |C_N/U(1)| = 2^{N^2+2N} \prod_{k=1}^N (4^k - 1). \quad (7)$$

Since the number of possible Clifford combinations for a single-qubit is not particularly demanding, being $|\overline{C_1}| = 24$, in this work, we have used all the possible unitaries to experimentally assess the fundamental quantities cited above

for single-qubit states. For two-qubits, instead, the number of possible products of single-qubit Clifford unitaries dramatically increases ($|\overline{C_1 \otimes C_1}| = 576$) and in general the cardinality grows as 24^N . To reduce the experimental effort in calculating two-qubit states and purities, we have randomly picked $N_{\text{rand}} = 400$ Clifford gates from the C_2 gate set, where N_{rand} is the number of randomizations.

For each choice of single-qubit Clifford C , we measure the readout probability vector $P(\mathbf{s}|C)$. The vector components of $P(\mathbf{s}|C)$ are obtained as the number of events n_s for which the measured output corresponds to the computational basis states represented by the bitstring \mathbf{s} normalized to the total number of shots measurements N_{shot} , $p_s = n_s/N_{\text{shot}}$. The state assignment process uses the discrimination threshold obtained by an initialization experiment, unique for each quantum state preparation.

Since \mathbb{E}_C represents the *sample mean* of $P(\mathbf{s}_l|C)$ over the number of Clifford gates N_C ,

$$\bar{x} = \mathbb{E}_C [x] \equiv \frac{1}{N_C} \sum_{i=1}^{N_C} x_i, \quad (8)$$

where x either represents purity \mathcal{P} and stabilizer purity \mathcal{W} , the *statistical sample variance* is calculated in terms of the square deviations from the mean $d_i^2 = (x_i - \bar{x})^2$ as

$$s^2 = \text{Var}(x) = \mathbb{E}_C [(x - \bar{x})^2] \equiv \frac{1}{N_C - 1} \sum_{i=1}^{N_C} (x_i - \bar{x})^2. \quad (9)$$

It follows that the *statistical sample standard deviation* is the square root $s = \text{Std}(x) = \sqrt{s^2}$, which represents, as usual, the spread of the experimental measurements. However, when taking a limited sample from a probability distribution, an inherent error is induced by the finite sampling. Therefore, we introduce the *sampling error*, defined in terms of the statistical sample standard deviation s as

$$\Delta x = \frac{s}{\sqrt{N_C}}. \quad (10)$$

Finally, given the non-linear (logarithm) function behavior of our random variables \mathcal{P} (purity) and \mathcal{W} (stabilizer purity), we are required to perform error propagation to get the average and statistical sampling error of Stabilizer Rényi entropy and 2-Rényi entropy. Using standard methods of error propagation, the estimator of the variance of a function f of two random variables x and y is given by

$$\begin{aligned} \text{Var}[f(x, y)] &\approx \left| \left(\frac{\partial f}{\partial x} \right)_{\bar{x}, \bar{y}} \right|^2 \text{Var}(x) \\ &\quad + \left| \left(\frac{\partial f}{\partial y} \right)_{\bar{x}, \bar{y}} \right|^2 \text{Var}(y) + 2 \left(\frac{\partial f}{\partial x} \frac{\partial f}{\partial y} \right)_{\bar{x}, \bar{y}} \text{Cov}(x, y), \end{aligned} \quad (11)$$

which for the SRE M_2 yields

$$\text{Var}(M_2) \approx \frac{\text{Var}(\mathcal{W})}{(\mathcal{W} \ln 2)^2} + \frac{\text{Var}(\mathcal{P})}{(\mathcal{P} \ln 2)^2} + 2 \frac{\text{Cov}(\mathcal{W}, \mathcal{P})}{\mathcal{W} \mathcal{P} (\ln 2)^2}. \quad (12)$$

However, in Ref. [18], it is shown that the covariance between \mathcal{P} and \mathcal{W} is exactly zero, so we can neglect that term in the expression, finally yielding

$$\Delta M_2 = \frac{1}{\ln 2} \sqrt{\frac{\text{Var}(\mathcal{W})}{N_C \bar{\mathcal{W}}^2} + \frac{\text{Var}(\mathcal{P})}{N_C \bar{\mathcal{P}}^2}}. \quad (13)$$

RDM purity from global measurement data

In case of the direct method for measuring non-local magic, we measure the subsystem purity $\mathcal{P}(\psi_A)$ with $\psi_A := \text{Tr}_B(|\psi\rangle\langle\psi|)$ to extract the value of the Schmidt coefficient. Analogously to the global system purity, partial purity can be measured via Randomized Clifford Measurements using the following formula [34]:

$$\mathcal{P}(\psi_A) = \mathbb{E}_C 2^{N_A} \sum_{s_A, s'_A} (-2)^{-\|\vec{s}_A\|_2} P(s_A|C) P(s'_A|C), \quad (14)$$

where the authors used generic randomized unitaries to compute this quantity. However, the same result holds if one restricts the unitary gate set to be taken from the Clifford group, as it is a unitary 3-design [52]. The prefactors in terms of Hamming weight of strings $\|\vec{s}\|$ are defined as $\|\vec{s}\|_2 = \sum_{i=1}^n s_1^i \oplus s_2^i$ where $\|\vec{s}\|$ where the \oplus symbol represents the modulo 2 sum or XOR between the bit strings. Note that in the RCM protocol the expression for evaluating the stabilizer purity involves the prefactor $\|\vec{s}\|_4$, involving XOR operations between 4 bit strings.

One recovers the subsystem probability outcomes as the marginal probability distributions of the global measurement outcomes, thereby using the same data taken to measure the purity and magic of the global state, as seen in the following calculation:

$$\begin{aligned} P_\psi(s) &= P(s_A, s_B) = \text{Tr}[\psi |s_A s_B\rangle\langle s_A s_B|] \\ &= \text{Tr}_A\{\text{Tr}_B[(\mathbb{1}_A \otimes |s_B\rangle\langle s_B|)\psi] |s_A\rangle\langle s_A|\} \\ &= \text{Tr}_A[\psi_A |s_A\rangle\langle s_A|] \text{Tr}_B[\psi_B |s_B\rangle\langle s_B|] \\ &= P_{\psi_A}(s_A) P_{\psi_B}(s_B). \end{aligned} \quad (15)$$

Therefore, summing over all possible outcomes of one of the two qubits we reconstruct the partial probability distribution on the other qubit as

$$P_{\psi_A}(s_A) = \sum_{s_B} P(s_A, s_B). \quad (16)$$

Initialization experiment

The initialization experiment involves the preparation of an N -qubit computational state $|i\rangle$. We then acquire simultaneously a readout voltage across each qubit readout resonator in the I, Q plane, and identify the state discrimination threshold as discussed in Ref.[53] by using the conditional probability method therein introduced. This also allows us to obtain the readout probability matrix, i.e. the probability to measure the state $|j\rangle$ over the computational basis states as the ratio between the number of counts in the different basis states n_{ij}^{init} and the total number of shots N_{shot} , $p_{ij}^{\text{init}} = n_{ij}^{\text{init}}/N_{\text{shot}}$. The readout probability matrix is finally used to calculate the readout fidelity per quantum circuit. In this work, we have

used $N_{\text{shot}} = 5000$ for determining the outcome probability distributions $P(s_i|C)$ for each given Clifford pair C .

Noise analysis

In this section, we explain the main sources of noise by which the chip is affected, and the techniques we used to mitigate and obtain an appropriate theoretical error model for the experimental data. We created a model without making use of free parameters, and only using independent benchmarking data of the quantum processor. As mentioned in the main text, we focused on two main sources, namely readout error in computational basis measurements, and depolarizing error on the CNOT (or rather, the CZ) gate, each of which we will tackle in a separate subsection.

Readout noise

Readout error means the expected outcomes of measurements do not necessarily correspond to the actual preparation. For example, if we prepare a two qubit state in $|00\rangle$ and we find it in $|10\rangle$ upon measurement, it means a readout error has occurred. The readout errors we encounter are of classical type, and come in different varieties: i) *uncorrelated* (no cross-talk); ii) *correlated*, which signals crosstalk, i.e., unwanted correlation between qubits existing on the quantum chip.

Formally, a quantum measurement is modeled through the use of Positive-Operator Valued Measurements (POVM), which are positive-semi-definite operators Π_x , one for each possible measurement outcome, that satisfy $\sum_x \Pi_x = \mathbb{1}$. The probability of getting an outcome x on a certain state preparation ρ is then given by the Born rule, namely $p_x = \text{Tr}[\Pi_x \rho]$. In the case of two qubits and a measurement in the computational basis, we have four POVMs, namely $\mathbf{M}^{\text{ideal}} = (\Pi_{00}, \Pi_{01}, \Pi_{10}, \Pi_{11})^T$, with $\Pi_{ij} = |ij\rangle\langle ij|$.

However, in the presence of readout noise, the measurement actually performed is a noisy POVMs, denoted $\mathbf{M}^{\text{noisy}}$, related to the ideal one through a left-stochastic matrix Λ , in the following way:

$$\mathbf{M}^{\text{noisy}} = \Lambda \cdot \mathbf{M}^{\text{ideal}}, \quad (17)$$

where Λ is usually referred to as *calibration* or *noise matrix*. Practically, the presence of readout noise induces a transformation on the would-be ideal outcome probabilities by the same matrix Λ , namely $\mathbf{p}^{\text{exp}} = \Lambda \cdot \mathbf{p}^{\text{ideal}}$, due to the linearity of the Born rule.

The calibration matrix is experimentally obtained by preparing states in the computational basis and measuring them in the same basis. The entries of Λ are then given by $\Lambda_{ij} = p(i|j)$, namely the probability of measuring the outcome j given that the preparation is in the state $|i\rangle$. In the ideal case, the calibration matrix should coincide with the identity matrix, i.e. one should not get outcomes different from the preparation. However, in the presence of readout noise this is not the case.

Given the calibration matrix, one would be tempted to just invert it to obtain the ideal probabilities in the post-processing of the data, and to some extent, this can work well when the objective of the experiment is the expectation value of an observable [54]. However, this is considered bad practice when the actual focus of the analysis is the vector

of outcomes probabilities, such as our case. The reason is that the inverse of a stochastic matrix is not positive in general; this means that applying this inverse matrix to the probability data may yield negative, non-physical probability vectors. To avoid this, we employ another post-processing, least-squares measuring filter method. This consists in computing the probabilities that minimize the distance between the measured ones given the noise matrix. The vectors obtained by this minimization are then used for the subsequent analysis. More explicitly, we compute

$$\mathbf{p}^{\text{mit}} := \underset{\mathbf{p} \geq 0, \sum p_i = 1}{\text{argmin}} \|\Lambda \cdot \mathbf{p} - \mathbf{p}^{\text{exp}}\|_2^2. \quad (18)$$

This method is straightforward, but difficult to scale to more than a few qubits, since in the case of correlated noise we need to store the entire $2^N \times 2^N$ calibration matrix in memory and perform a minimization procedure over a $(2^N - 1)$ -dimensional space of probabilities. However, since the number of qubits involved in our experiments is either one or two, this method is easily implementable and quick. In case of larger qubit number, other methods may be implemented [54–60].

Depolarizing noise

On the prediction side, we account for the presence of depolarizing noise on the CNOT gate (or rather, the CZ since it is the native gate of our processor, which explains the lower gate fidelity compared to the single qubit ones. The action of the depolarizing noise channel on a state ρ is described as follows[61]:

$$\mathcal{E}_{\text{dep}}(\rho) := p_{\text{dep}} \rho + (1 - p_{\text{dep}}) \frac{\mathbb{1}}{d}, \quad (19)$$

which means that with a probability $1 - p_{\text{dep}}$ the initial state is mapped to the completely mixed state, whereas with probability p_{dep} the state remains unchanged. We used the respective parameters of depolarizing noise, which correspond exactly to the survival probability p_1 of the Interleaved Randomized Benchmarking [38] seen in Eq. S4 in *Supplemental Information* for each experiment.

Supplementary information. The article is accompanied by supplemental information.

Acknowledgements. The authors thank Lorenzo Campos Venuti for useful discussion, Hany Ali, Alessandro Bruno, Johannes Hermann, and Christian Junger for support on the gate calibrations.

Declarations

Funding

The work is supported by the PNRR MUR project PE0000023-NQSTI and the PNRR MUR project CN 00000013-ICSC.

Author contribution

These authors contributed equally: H.G.A. and G.E.. H.G.A. and G.E. developed the experimental protocol; V.S., C.C., A.S. and H.G.A. characterized and calibrated the device; V.S., H.G.A., C.C. and A.S. performed and analyzed

the experiments; G.E. and J.O. analyzed the data; G.E. and J.O. developed the error mitigation scheme used for data analysis. A.H. conceived and supervised the project. All authors contributed to the interpretation of the results and production of the paper.

Circuit	Qubit	$F_{RO}(\%)$	$F_{RB}(\%)$	$T_2^{\text{echo}}(\mu\text{s})$	$T_2^*(\mu\text{s})$	$T_1(\mu\text{s})$	state	$M_2 (= \mathbf{0})$	$M_2 (\neq \mathbf{0})$
Fig. 1(c)	D3	96 ± 1	99.75 ± 0.01	34 ± 2	24 ± 1	30 ± 1	$ \psi_0\rangle$	0.1 ± 0.3	
		97 ± 1	99.910 ± 0.002	38 ± 1	34 ± 4	30.0 ± 0.4	$ \psi_1\rangle$	0.0 ± 0.3	0.43 ± 0.12
	C4	94 ± 1	99.925 ± 0.002	42 ± 1	21 ± 1	36 ± 2		0.0 ± 0.3	0.42 ± 0.12
	C4	94 ± 1	99.925 ± 0.002	42 ± 1	21 ± 1	36 ± 2	$ \psi_2\rangle$	0.0 ± 0.3	0.39 ± 0.14
Fig. 1(d)		97 ± 1	99.910 ± 0.002	38 ± 1	34 ± 4	30.0 ± 0.4		0.0 ± 0.3	0.43 ± 0.12
D3	97 ± 1	99.910 ± 0.002	38 ± 1	34 ± 4	30.0 ± 0.4		0.0 ± 0.3	0.40 ± 0.13	
		$F_{RO}(\%)$	$F_{RB}(\%)$	$F_{RB}^{\text{CZ}}(\%)$	$C^{\text{MW}}(\%)$	$C^{\text{ZZ}}(\text{kHz})$			
Fig. 1(e)	D3 C4	92 ± 1	99.75 ± 0.01	98 ± 2	~ 0.12	~ 100	$ \psi_3\rangle$	0.1 ± 0.1	0.85 ± 0.05
Fig. 1(f)		92 ± 1	99.905 ± 0.003		~ 1.57		$ \psi_4\rangle$	0.2 ± 0.1	

Extended Data Table 1: Experimental magic measured for the quantum states in Fig. 1. Systematic investigation of experimental magic for single and two-qubit quantum states, for qubits D3 and C4, as a function of: the readout fidelity F_{RO} , the average single-qubit gates fidelity from Randomized Benchmarking F_{RB} , relaxation, Ramsey and Echo coherence times (T_1 , T_2^* and T_2^{Echo} , respectively). For two-qubit circuits, we report an estimation of the drive and ZZ crosstalk, C^{MW} and C^{ZZ} respectively, on the investigated pair. The final columns refers measured magic for the states after introduction of T gates and in the circuits are denoted as $|\psi_i^T\rangle$. Discussion on error estimation is in *Methods*.

Supplemental Information for "Experimental demonstration of non-local magic in a superconducting quantum processor"

S1 Experimental setup

The fridge employed in this work is a dry dilution refrigerator BlueforsXLS1000SL, with minimal base temperature of 7 mK . It is equipped with microwave coaxial cables, which allow operation within the microwave frequency range (DC-18GHz, nominally). The cryostat features four types of cryogenic lines: input and output lines for the readout, drive lines for qubit control, and flux lines for frequency tuning with either static or pulsed external magnetic flux. Feedline and drive lines feature a nominal attenuation of -60dB , which adds to -10dB attenuation of the line itself (stainless steel) and infrared low-pass filters with a cutoff of about 10GHz . The flux lines are equipped with -20dB nominal attenuation, anchored at 4K to prevent Joule heating, and two infrared low-pass filters in series of 10GHz and 1GHz . Flux lines are in stainless steel from room temperature to the 4K plate, and in niobium titanium below 4K . This allows for reducing heat dissipation when delivering static currents up to 40mA , used to generate magnetic flux on chip. The output lines, also made of niobium titanium below 4K and in copper-nickel at highest temperatures, are not attenuated, and include a 10GHz low-pass filter and a Low-Noise Factory LNF-ISC double junction isolator at the mixing chamber (MXC), so that signals from room-temperature towards the sample are attenuated nominally by a total of 40 dB . Since the output signals of the qubits are single-photon signals, amplifiers are required. In our system, there are two amplification stages. There is a High Electron Mobility Transistor (HEMT) with nominal amplification of 40dB on the 4K plate, and three amplifiers at room temperature with a nominal 16dB amplification each. The cryogenic setup is shown in Figure S1. Finally, to

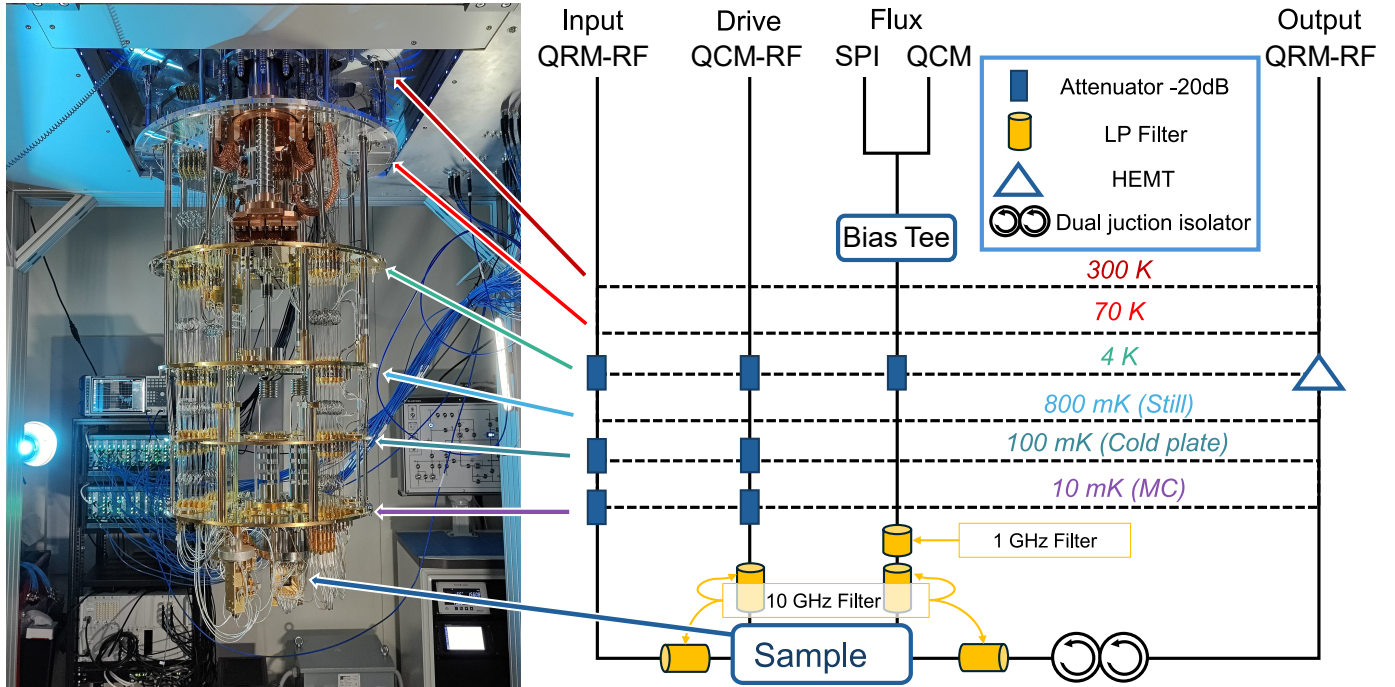


Fig. S1: Cryogenic setup scheme, including the attenuation scheme for the input, drive and flux lines. On the output line, there are a dual junction isolator and an HEMT amplifier. Each line has a low-pass filter.

provide combined static and pulsed magnetic flux through the flux lines, we employ bias-tees at room temperature, where the DC signal is generated by Qblox S4g modules (installed in a Qblox SPI-rack) and the RF signal is generated by a Qubit Control Module (QCM). This generates output signals up to 400 MHz , and are installed in a Qblox Cluster, a room-temperature microwave modular electronics fully interfaceable with Python packages, thanks to the open-source package Quantify [62]. The modules used for the measurements of this work are:

- Qubit Readout Module RF (QRM-RF), which allows generation of output multi-tone signals for multiplexed readout up to 18.5 GHz , and to demodulate the readout signals over a 400 MHz bandwidth;
- Qubit Control Module RF (QCM-RF), which allows output signals up to 18.5 GHz ;
- Qubit Control Module (QCM), which generates pulses in the baseband regime up to 400 MHz .

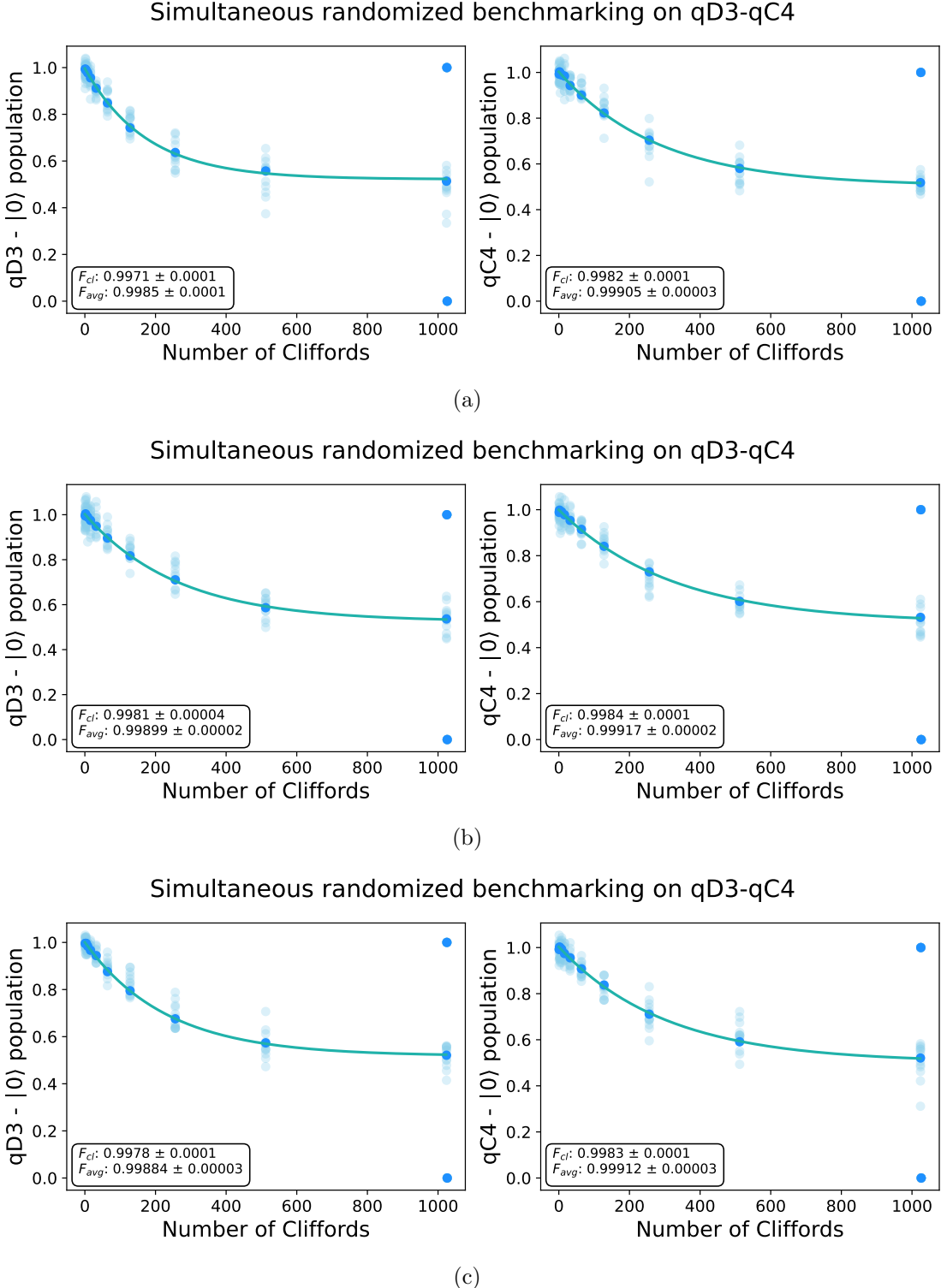


Fig. S2: Simultaneous Randomized Benchmarking for single-qubit gate fidelity on qubit qD3 and qC4 for the three proposed experiment: the RB in (a) for the LM state experiment, in (b) for the M state, and in (c) for the NLM state. Blue scatter data corresponds to the population of the $|0\rangle$ state as a function of the number of Clifford gates in the randomized benchmarking sequence, averaged over 50 random seeds. The solid line represents the fit function (Eq. (S1)) used for the estimation of the single-qubit randomized benchmarking average gate fidelity.

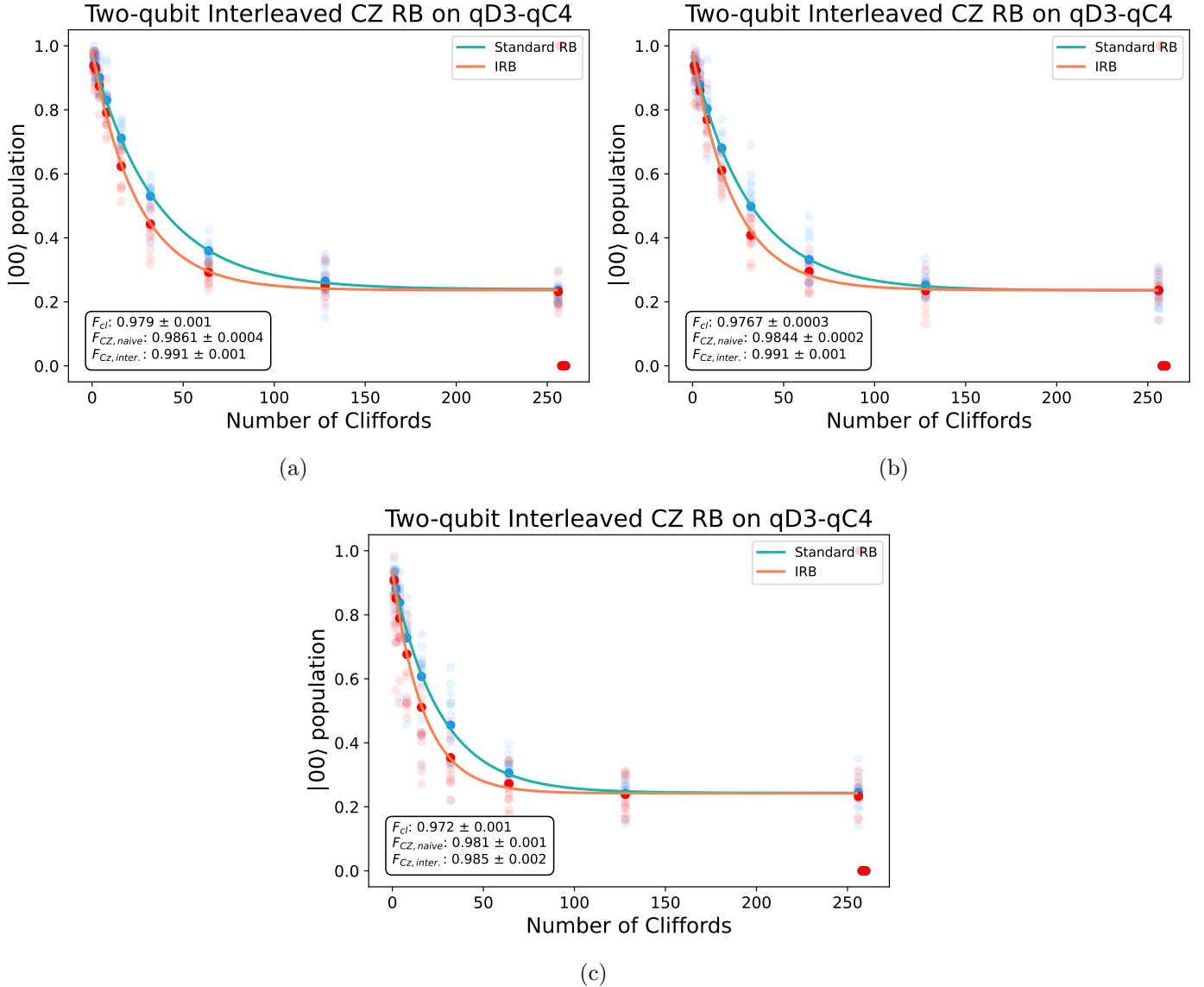


Fig. S3: Interleaved Randomized Benchmarking for the CZ gate on qubit qD3 and qC4 for the three proposed experiment: the CZ-IRB in (a) for the LM state experiment, in (b) for the M state, and in (c) for the NLM state. The scatter data correspond to the population of the $|00\rangle$ state as a function of the number of Clifford gates in the randomized benchmarking sequence, averaged over 50 random seeds. The solid line represents the fit function (Eq.(S1)) used for the estimation of survival probabilities. Specifically, the blue line refers to the standard simultaneous RB, while the orange one refers to the IRB, from which it is possible to estimate p_0 and p_1 , respectively. From the two survival probabilities, the fidelity of the CZ can be obtain according to Eq.(S4).

S2 Benchmarking protocols and experiments

S2.1 Single and two-qubit gates optimization protocols

Before the experimental measurements of magic on the investigated D3-C4 pair, we have performed: i) single- and two-qubits gate calibrations [63, 64], ii) simultaneous readout calibration. In detail, the experimental single-qubit gate set includes rotations $R_{xy}(\theta)$, where the rotation angle θ is controlled by changing the amplitude of drive DRAG (Derivative Reduction Adiabatic Gate) pulses [43, 65, 66] with a fixed duration of 60 ns. After a rough estimation of the amplitude required to perform a transition from the ground to the excited state of the qubits (π -pulse) with Rabi oscillations experiments [43], we have optimized the pulses frequency by using Ramsey oscillations experiments [43], the shape through Motzoi protocol [67] and we performed a fine tuning of the π -pulse amplitude through the flipping protocol. This sequence of optimization steps is finally tested through simultaneous All-XY experiments, able to recover error syndromes in X-Y gates (e.g., detuning, amplitude and DRAG errors), and eventually allowing us to correct for specific errors when they occur [64].

As for the two-qubit gates calibration, we have focused on CZ gates implemented through flux-pulses able to set on resonance the high-frequency qubit (D3) with the low-frequency qubit (C4). We used the cryoscope technique to correct for flux pulses distortions [68], and CZ-Chevron experiments employing unipolar flux pulses to get a rough estimation of the amplitude and the duration of the CZ flux pulses [43, 44]. Then, we have used Sudden-Net Zero (SNZ) flux pulses, whose parameters have been optimized through conditional oscillations experiments [69] (Sec. S2). By measuring landscapes of the conditional two-qubit phase and the leakage as a function of the amplitude and the shape of the SNZ pulses, as well as the flux sweet spot of the qubits, we aimed at the minimum leakage and a conditional phase as close as possible to the nominal 180° conditional two-qubit phase [44]. Finally, we have also corrected for the single-qubit phases to enhance the fidelity of the CZ gates [44].

The readout calibration procedure, instead, involved Single-Shot Readout (SSRO) experiments [70] as a function of the power and the frequency of the readout tone, as well as the duration of the readout signal and the integration time. Single-shot readout is performed suddenly before any quantum circuit implemented, and is used to identify the discrimination threshold for the computational basis state and the calculation of the count vectors and the readout state probability [53]. Finally, besides standard coherence times benchmarking, e.g. relaxation, Ramsey and Hahn-Echo coherence times (T_1 , T_2^* and T_2) [43], simultaneous single-qubit Randomized Benchmarking (RB) [71] and CZ Interleaved two-qubits RB (IRB) [38, 72] were used to estimate the average Clifford gate fidelities for the two qubits and the average CZ gate fidelity (App. S2), while SSRO experiments have been used to estimate the readout fidelity [53].

In the context of RCM, $C = \bigotimes_{i=1}^N C_i$ represents the tensor product of N single-qubit Clifford unitaries C_i , each randomly sampled from the ensemble of unitaries, which includes X , Y , Z , H , and S gates, plus the trivial identity gate I , and all 24 of their possible combinations. While X , Y and Z gates are directly related to microwave/flux pulses [43], H and S gates are decomposed in terms of R_x , R_y , and R_z gates. For example, H is decomposed in terms of $R_y(\pi/2)R_z(\pi)$ rotations, while S is implemented as a $R_z(\pi/2)$ pulse, where $R_y(\theta) \equiv R_{xy}(\theta, \frac{\pi}{2})$, $R_z(\theta) = e^{-i\frac{\theta}{2}Z}$. The T is implemented as $R_z(\pi/4)$. CNOT is implemented as $\text{CNOT}_{1 \rightarrow 2} = (I \otimes H) \cdot \text{CZ}_{1 \rightarrow 2} \cdot (I \otimes H)$.

S2.2 Fidelity estimation

Randomized Benchmarking (RB) is a class of methods used to evaluate the fidelity of applied gates and is based on the implementation of sequences of random gate operations [73–75]. The advantages of RB protocols are their efficient scalability with the number of qubits n and the fact that they account for State Preparation and Measurement (SPAM) errors. In our protocol, the RB has been implemented over the Clifford gate set. Clifford based RB has several variants. Specifically, we focused on the Standard RB and the Interleaved RB (IRB).

S2.2.1 Single qubit Randomized Benchmarking

Standard Clifford RB is performed by initializing the qubit in the $|0\rangle$ state, followed by the application of a sequence of N_{cl} random Clifford gates, and then the inverse of all applied gates. Ideally, this sequence acts as the identity gate. However, due to gate errors, the final state will differ from the ideal one. Finally, we can thus extract the fidelity of the gates by comparing how close the final state is to the initial one. The survival probability p can be obtained by fitting the population of the $|0\rangle$ state as a function of the number of Clifford, using the exponential decay [76]:

$$F_{|0\rangle}(N_{\text{cl}}) = A \cdot p^{N_{\text{cl}}} + B, \quad (\text{S1})$$

where N_{cl} is the number of Clifford gates in the sequence. Given $d = 2^n$ as the dimensionality of the system for n qubits, the average gate fidelity can be estimated from the survival probability as:

$$F_{\text{avg.gate}} = (F_{\text{cl}})^{\frac{1}{1.875}}, \quad (\text{S2})$$

where

$$F_{\text{cl}} = 1 - \left(\frac{d-1}{d} - (1-p) \right). \quad (\text{S3})$$

This protocol was performed simultaneously on both qubits, qD3 and qC4. The single-qubit gate for each qubit was chosen randomly and independently from the single-qubit Clifford group, i.e., the protocol required applying the product of the single-qubit Clifford unitaries to the two-qubit register. An example of the protocol applied simultaneously on qubits D3 and C4 is shown in Fig. S2.

S2.2.2 CZ - Interleaved Randomized Benchmarking

The Interleaved Randomized Benchmarking (IRB) is a scalable experimental protocol for estimating the average error of individual quantum computational gates. The protocol involves interleaving random Clifford gates with the gate of interest, i.e., the CZ gate in our case [38]. This protocol is composed of three steps [38]:

- perform standard randomized benchmarking (RB) by choosing K sequences of random gates, where the first m gates in each sequence are selected randomly from the Clifford group, and the $(m+1)$ -th gate is the inverse of the composition of the first m gates. By fitting the exponential decay, we can obtain the survival probability p_0 (Eq.(S1));

- choose K sequences of Clifford elements where the first Clifford, in each sequence, is chosen randomly for the Clifford group, while the second is always the CZ gate, and alternate between random Clifford and the CZ gate up to m -th random gate. The $(m + 1)$ -th gate is the inverse of the composition of the first m gates and the m CZ gates. As well as for the standard RB, we can use the exponential decay fit to estimate the survival probability p_1 ;
- estimate the fidelity for the CZ gate as follow:

$$F_{\text{CZ,int}} = 1 - \left(\frac{d-1}{d} \cdot \left(1 - \frac{p_1}{p_0} \right) \right) \quad (\text{S4})$$

An example of the CZ-IRB performed on D3 and C4 is shown in Fig. S3. Moreover, we performed statistical measurements of the interleaved CZ gate fidelity, obtaining an average fidelity of $(98 \pm 2)\%$. The results are shown in Fig. S4.

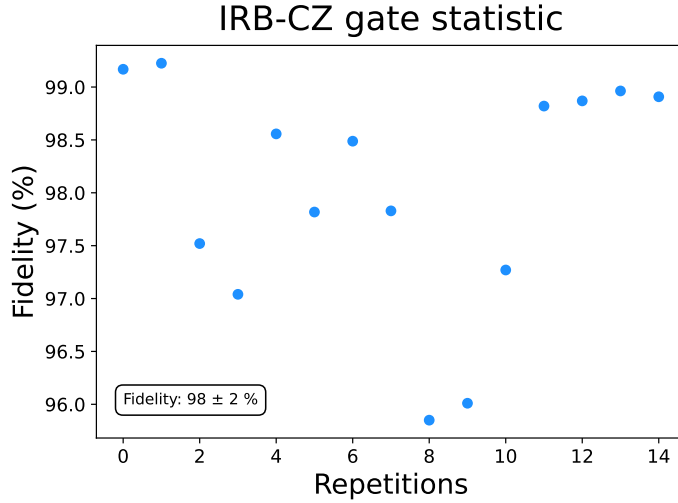


Fig. S4: Statistical measurements of the interleaved CZ gate fidelity.

S2.3 Crosstalk measurements

Crosstalk phenomena refer to interactions between qubits that can introduce noise into the system, leading to errors in algorithm implementation. Therefore, as a preliminary step, it is necessary to study the crosstalk affecting the device. There are various types of crosstalk, but in this work, we specifically focus on microwave crosstalk and ZZ crosstalk.

S2.3.1 Microwave crosstalk

To determine the microwave crosstalk strength from one qubit to another, we send a microwave pulse to the driveline of one qubit and measure its effect on the other qubit, referred to as the 'driven' and 'measured' qubit, respectively. Specifically, we perform a Rabi experiment on the driven qubit by sending a π -pulse at the frequency of the measured qubit and carry out a dispersive measurement on the latter. By using a sinusoidal fit, we can extract the π -pulse amplitude obtained from the experiment, which allows us to estimate the strength of the microwave crosstalk coefficient. Specifically, it can be estimated as:

$$C_{i \rightarrow j} = \frac{A_{j \rightarrow j} t_{j \rightarrow j}}{A_{i \rightarrow j} t_{i \rightarrow j}} \quad (\text{S5})$$

where $A_{i \rightarrow j}$ and $t_{i \rightarrow j}$ are the amplitude and duration of the π -pulse sent on qubit i and measured on qubit j , respectively. The microwave crosstalk matrix for the couple D3-C4 is shown in Fig. S5.

S2.3.2 ZZ crosstalk

By performing two-qubit gates, we introduce a controlled interaction between the two qubits. However, there may also be a small undesired coupling between them, which persists even when the controlled interaction is turned off. The effect of this interaction, known as residual ZZ coupling [68], is that the frequency of the $|0\rangle \rightarrow |1\rangle$ transition of one qubit shifts depending on the state of the other. In order to estimate the strength of this interaction, we can use a Ramsey-type experiment. Specifically, we perform a Ramsey sequence on the target qubit with an echo pulse at the midway point. In the meanwhile, the spectator qubit is prepared in the ground state for half of the sequence, and in the excited state for the second half. The pulse scheme of the experiment is shown in Fig. S6.

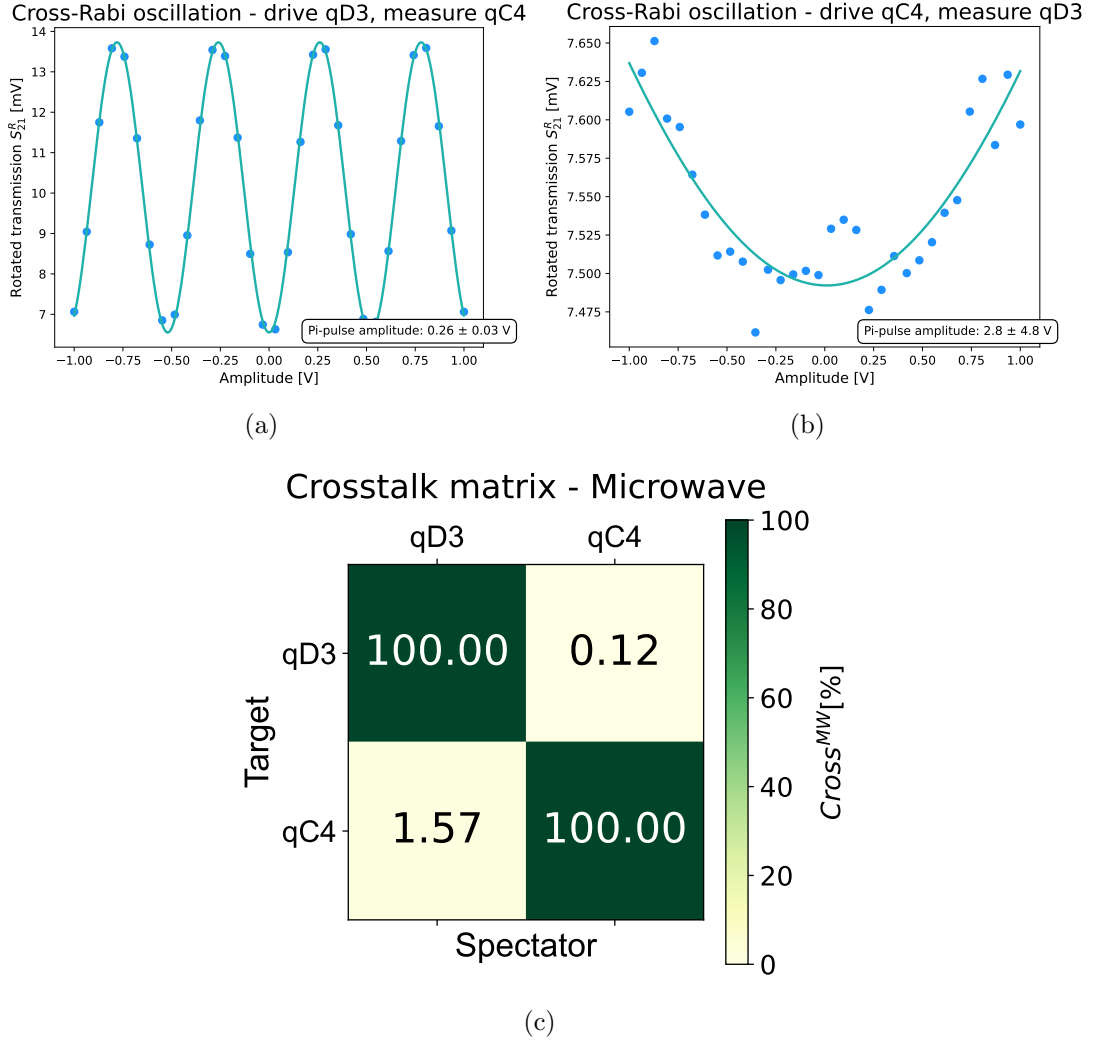


Fig. S5: Measurement of the MW crosstalk between qD3 and qC4. In (a) and (b), the results of the Rabi protocol performed using qD3 as the driven qubit and qC4 as the measured one, and vice versa, respectively. In (c), the MW crosstalk matrix for qD3 and qC4. The x- and y-axis indicates the measured qubit and the driven one. The colorbar represents the percentage of MW crosstalk.

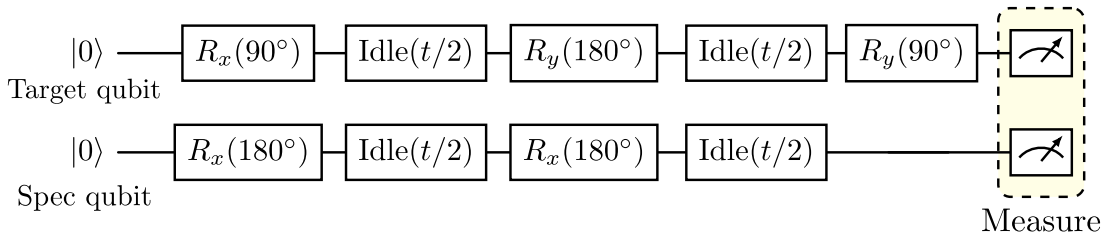


Fig. S6: Pulse sequence for ZZ residual coupling estimation. First, a $R_x(\pi/2)$ and $R_x(\pi)$ gates are applied on the target and the spectator qubit, respectively. The qubits are allowed to evolve freely for a variable delay $t/2$, after which a $R_y(\pi)$ and $R_x(\pi)$ rotation are applied on the target and spectator qubit, respectively. After waiting again for a variable delay $t/2$, a $R_y(\pi/2)$ pulse is applied on the target qubit. Finally, the circuit's output is measured.

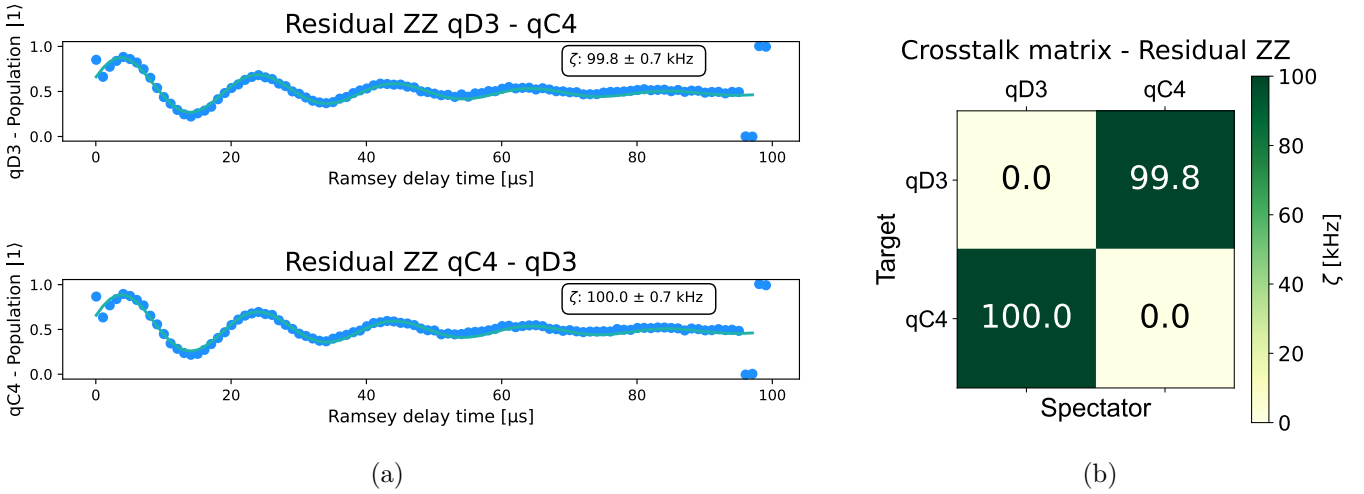


Fig. S7: Measurement of the ZZ residual coupling between qD3 and qC4. In (a) and (b) the population of the $|1\rangle$ state using qD3 and qC4 as target, respectively. The solid lines represent the fit function used to estimate the ZZ residual coupling. In (c), the ZZ crosstalk matrix for qD3 and qC4. The x- and y-axis indicates the spectator and the target qubit, respectively. The colorbar represents the shift in frequency due to the ZZ interaction.

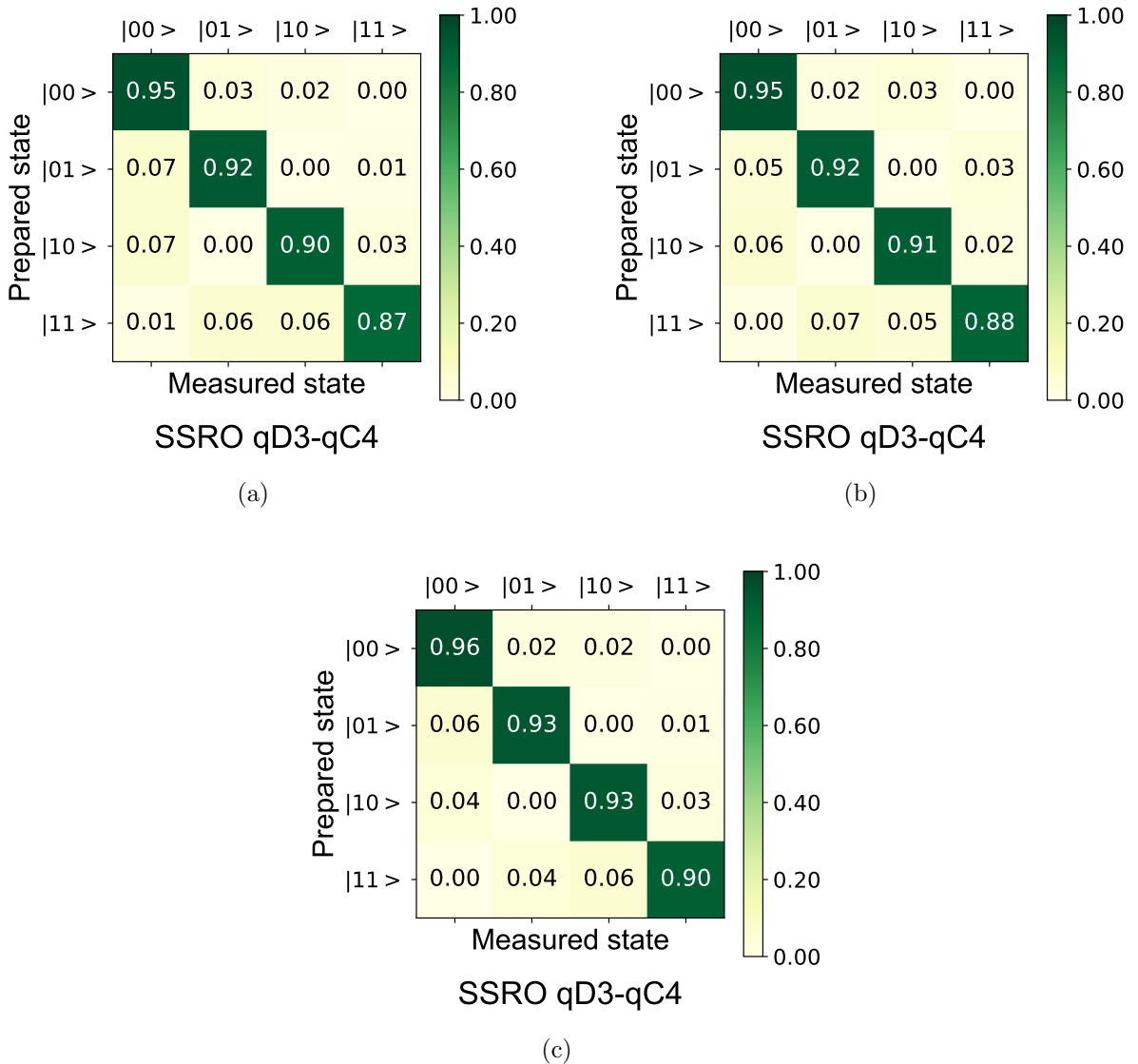


Fig. S8: Supplemental Figure – Initialization/assignment probability matrices. Initialization matrix for the three proposed experiments: in (a) for the LM state experiment, in (b) for the M state, and in (c) for the NLM state. The x- and y-axis indicate the measured and prepared state, respectively.

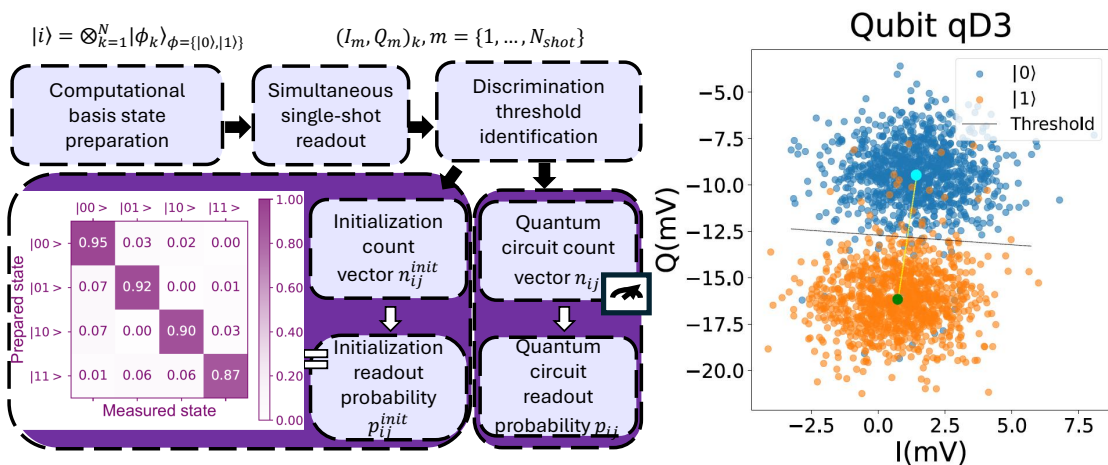
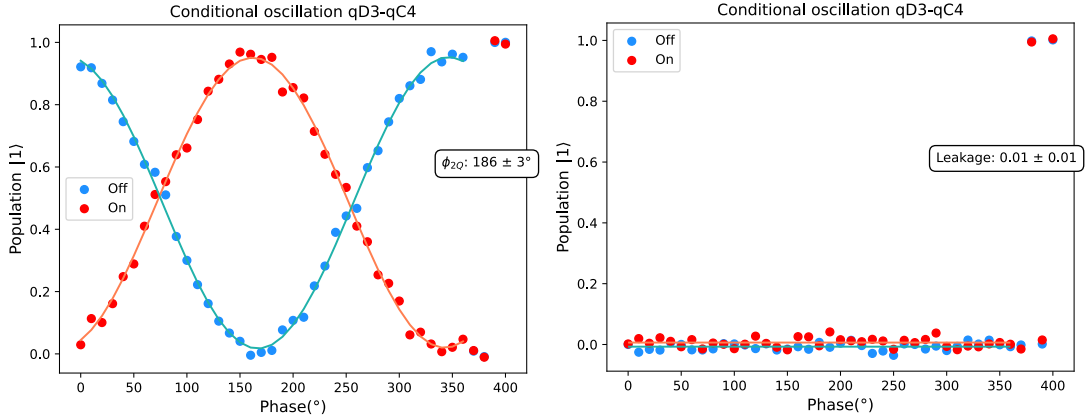
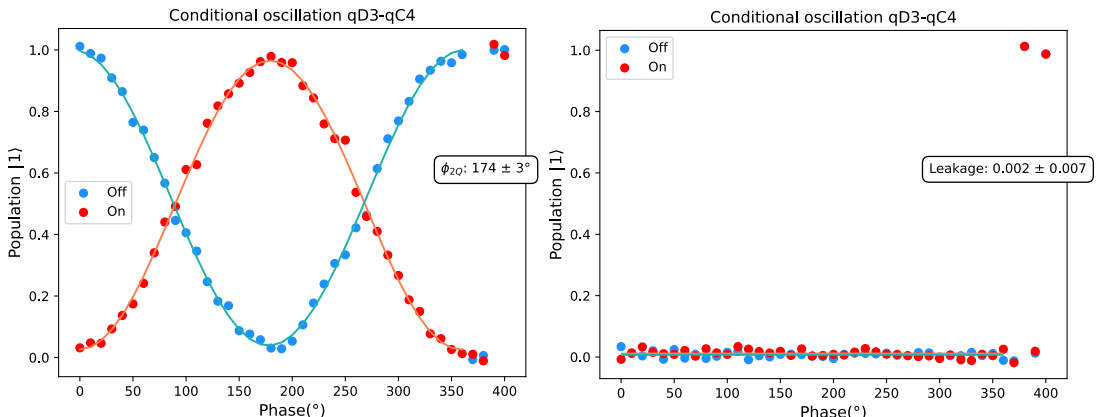


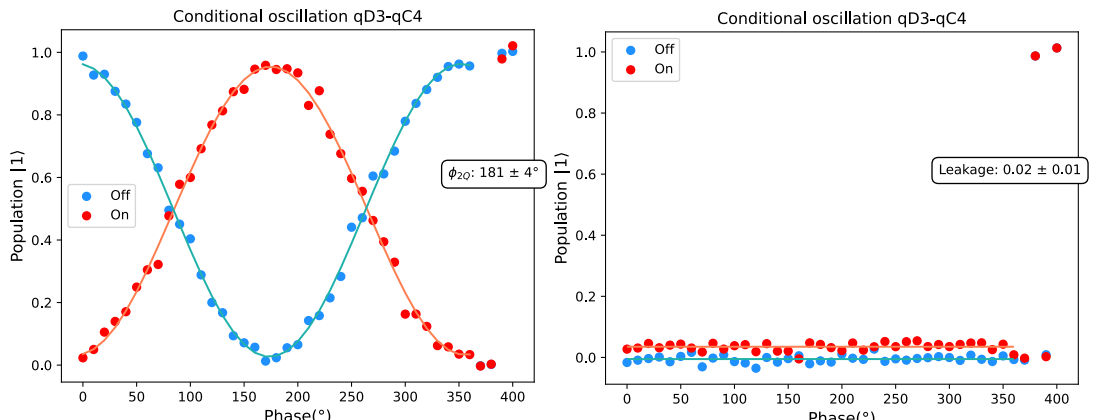
Fig. S9: Supplemental Figure - Experimental randomized protocol for magic measurements. In (a), a schematic representation of the randomized measurement protocol. In (b), the steps involved in the initialization experiment are performed before any quantum circuit. The initialization procedure is used on one hand to calculate the readout fidelity, but most importantly the computational basis states discrimination threshold (black dashed line in the top right inset). This allows to determine the output of any randomized Clifford circuit performed after the preparation of a quantum state.



(a)



(b)



(c)

Fig. S10: The measured $|1\rangle$ population as a function of the phase on qD3 on the left and on qC4 on the right for the three proposed experiment: in (a) for the LM state experiment, in (b) for the M state, and in (c) for the NLM state. The blue scatter data represent the measured values for the Off variant, while the orange ones the measured values for the On variant. The solid lines represent the fit function used to estimate the two-qubit phase θ_{2Q} on the left and the leakage L on the right.

Due to the residual ZZ interaction, the target qubit will acquire a phase. By varying the delay in the experiment, we observe an oscillation in the target qubit population, from which it is possible to estimate the residual ZZ coupling frequency. The ZZ-crosstalk matrix for the couple D3-C4 is shown in Fig. S7.

S2.4 Conditional oscillation

To tune up the CZ gate, it is possible to perform the conditional oscillation experiment. It can be used to measure the conditional phase θ_{2Q} acquired during an uncalibrated CZ gate, and to estimate the leakage L , defined as the average probability that a random computational state leaks out of the computational subspace [77]. In the conditional oscillation experiment, two variants of the same experiment are performed [69]. In the first variant (Off), a $\pi/2$ -pulse is applied on the target qubit, while the control qubit is left in the ground state. After that, the CZ flux pulse is applied. Finally, another $\pi/2$ -pulse is applied on the target before measuring the state of both qubits simultaneously. In the second variant (On), the control qubit is rotated into the excited state before applying the CZ gate. Then, the control qubit is pulsed back to the ground state before measuring both qubits. The difference in phase acquired by the target in the On and Off variants yields θ_{2Q} , while the population difference on the control, defined as the missing fraction m , allows us to estimate the leakage as $L = m/2$. In order to optimize θ_{2Q} , i.e. to have it equal to π , and to minimize the leakage L , the flux pulse amplitude and duration are changed. An example of the protocol performed for the CZ between D3 and C4 is shown in Fig. S10.

S3 Local magic distillation lemma

Lemma 1 (Local magic distillation). *Given a state $|\psi\rangle \in \mathcal{H} = \mathcal{H}_A \otimes \mathcal{H}_B$, an ancillary system in $|0\rangle$, and a Clifford unitary C such that*

$$C(|\psi\rangle \otimes |0\rangle) = |\psi'\rangle \otimes |\phi\rangle, \quad (\text{S6})$$

with $M_2(|\phi\rangle) > M^L(|\psi\rangle)$, then C does not allow a decomposition in local unitary operators on $\mathcal{H}_A \otimes \mathcal{H}_B$, namely it cannot be of the form $C = C_A \otimes C_{BC}$ or $C = C_B \otimes C_{AC}$.

Proof Since $C \in \mathcal{C}$, then $M_2(|\psi'\rangle \otimes |\phi\rangle) = M_2(|\psi\rangle)$. Since M_2 is additive, it holds that

$$\begin{aligned} M_2(|\psi'\rangle) + M_2(|\phi\rangle) &= M_2(|\psi\rangle) \\ &= M^{\text{NL}}(|\psi\rangle) + M^L(|\psi\rangle) \implies M_2(|\psi'\rangle) \\ &= M^{\text{NL}}(|\psi\rangle) + M^L(|\psi\rangle) - M_2(|\phi\rangle) \end{aligned} \quad (\text{S7})$$

by hypothesis, $M_2(|\phi\rangle) > M^L(|\psi\rangle)$, hence $M^L(|\psi\rangle) - M_2(|\phi\rangle) < 0$: thus we have

$$M_2(|\psi'\rangle) < M^{\text{NL}}(|\psi\rangle) = \min_{U_A, U_B} M_2[(U_A \otimes U_B) |\psi\rangle] \quad (\text{S8})$$

proving that $|\psi'\rangle$ cannot be the output of the product of local unitaries on A and B . \square

References

- [1] Aaronson, S. & Gottesman, D. Improved simulation of stabilizer circuits. *Phys. Rev. A* **70**, 052328 (2004). URL <https://link.aps.org/doi/10.1103/PhysRevA.70.052328>.
- [2] Bravyi, S. & Kitaev, A. Universal quantum computation with ideal Clifford gates and noisy ancillas. *Physical Review A* **71**, 022316 (2005).
- [3] Veitch, V., Hamed Mousavian, S. A., Gottesman, D. & Emerson, J. The resource theory of stabilizer quantum computation. *New Journal of Physics* **16**, 013009 (2014).
- [4] Li, G.-C. *et al.* Invested and potential magic resources in measurement-based quantum computation. *Phys. Rev. Lett.* **135**, 160203 (2025). URL <https://link.aps.org/doi/10.1103/4yyv-hggz>.
- [5] Qian, D. & Wang, J. Quantum nonlocal nonstabilizerness. *Physical Review A* **111**, 052443 (2025).
- [6] Leone, L., Oliviero, S. F. E., Zhou, Y. & Hamma, A. Quantum chaos is quantum. *Quantum* **5**, 453 (2021).
- [7] Zhou, S., Yang, Z.-C., Hamma, A. & Chamon, C. Single T gate in a Clifford circuit drives transition to universal entanglement spectrum statistics. *SciPost Phys.* **9**, 087 (2020). URL <https://scipost.org/10.21468/SciPostPhys.9.6.087>.
- [8] True, S. & Hamma, A. Transitions in entanglement complexity in random circuits. *Quantum* **6**, 818 (2022).
- [9] Leone, L., Oliviero, S. F. E., Esposito, G. & Hamma, A. Phase transition in stabilizer entropy and efficient purity estimation. *Physical Review A* **109**, 032403 (2024).
- [10] Oliviero, S. F. E., Leone, L., Lloyd, S. & Hamma, A. Unscrambling quantum information with Clifford decoders. *Physical Review Letters* **132**, 080402 (2024).
- [11] Feynman, R. P. Simulating physics with computers. *International Journal of Theoretical Physics* **21**, 467–488 (1982).
- [12] Shor, P. W. Polynomial-time algorithms for prime factorization and discrete logarithms on a quantum computer. *SIAM Journal on Computing* **26**, 1484–1509 (1997).
- [13] Harrow, A. W., Hassidim, A. & Lloyd, S. Quantum algorithm for linear systems of equations. *Physical Review Letters* **103**, 150502 (2009).
- [14] Lloyd, S. Universal quantum simulators. *Science* **273**, 1073–1078 (1996).
- [15] Grover, L. K. Quantum mechanics helps in searching for a needle in a haystack. *Physical Review Letters* **79**, 325–328 (1997).
- [16] Gottesman, D. The Heisenberg representation of quantum computers (1998). URL <https://arxiv.org/abs/quant-ph/9807006>. arXiv:quant-ph/9807006.
- [17] Howard, M. & Campbell, E. Application of a resource theory for magic states to fault-tolerant quantum computing. *Physical Review Letters* **118**, 090501 (2017).
- [18] Iannotti, D., Esposito, G., Campos Venuti, L. & Hamma, A. Entanglement and Stabilizer entropies of random bipartite pure quantum states. *Quantum* **9**, 1797 (2025). URL <https://doi.org/10.22331/q-2025-07-21-1797>.
- [19] Tirrito, E. *et al.* Quantifying nonstabilizerness through entanglement spectrum flatness. *Phys. Rev. A* **109**, L040401 (2024). URL <https://link.aps.org/doi/10.1103/PhysRevA.109.L040401>.
- [20] Szombathy, D., Valli, A., Moca, C. P., Farkas, L. & Zaránd, G. Independent stabilizer rényi entropy and entanglement fluctuations in random unitary circuits (2025). URL <http://arxiv.org/abs/2501.11489>. ArXiv:2501.11489 [quant-ph].
- [21] Korbany, D. A., Gullans, M. J. & Piroli, L. Long-range nonstabilizerness and phases of matter. *Phys. Rev. Lett.* **135**, 160404 (2025). URL <https://link.aps.org/doi/10.1103/1hlj-h6t9>.
- [22] Odavić, J., Viscardi, M. & Hamma, A. Stabilizer entropy in nonintegrable quantum evolutions. *Physical Review B* **112**, 104301 (2025).
- [23] Cao, C. *et al.* Gravitational back-reaction is magical (2024). URL <http://arxiv.org/abs/2403.07056>.

[24] Preskill, J. Quantum computing in the NISQ era and beyond. *Quantum* **2**, 79 (2018). URL <https://doi.org/10.22331/q-2018-08-06-79>.

[25] Odavić, J. *et al.* Complexity of frustration: A new source of non-local non-stabilizerness. *SciPost Physics* **15**, 131 (2023).

[26] Wills, A., Hsieh, M.-H. & Yamasaki, H. Constant-overhead magic state distillation. *Nature Physics* (2025). URL <https://doi.org/10.1038/s41567-025-03026-0>.

[27] Sales Rodriguez, P. *et al.* Experimental demonstration of logical magic state distillation. *Nature* (2025). URL <https://doi.org/10.1038/s41586-025-09367-3>.

[28] Cusumano, S. *et al.* Non-stabilizerness and violations of CHSH inequalities (2025). URL <https://arxiv.org/abs/2504.03351>. arXiv:2504.03351.

[29] Pastawski, F., Yoshida, B., Harlow, D. & Preskill, J. Holographic quantum error-correcting codes: toy models for the bulk/boundary correspondence. *Journal of High Energy Physics* **2015**, 149 (2015).

[30] Leone, L., Oliviero, S. F. & Hamma, A. Stabilizer Renyi entropy. *Physical Review Letters* **128**, 050402 (2022).

[31] Leone, L. & Bittel, L. Stabilizer entropies are monotones for magic-state resource theory. *Physical Review A* **110**, L040403 (2024).

[32] Oliviero, S. F. E., Leone, L., Hamma, A. & Lloyd, S. Measuring magic on a quantum processor. *npj Quantum Information* **8**, 1–8 (2022). URL <https://www.nature.com/articles/s41534-022-00666-5>.

[33] Elben, A. *et al.* The randomized measurement toolbox. *Nature Reviews Physics* **5**, 9–24 (2022).

[34] Brydges, T. *et al.* Probing Rényi entanglement entropy via randomized measurements. *Science* **364**, 260–263 (2019). URL <https://www.science.org/doi/10.1126/science.aau4963>.

[35] Cai, Z. *et al.* Quantum error mitigation. *Rev. Mod. Phys.* **95**, 045005 (2023). URL <https://link.aps.org/doi/10.1103/RevModPhys.95.045005>.

[36] Ahmad, H. G. *et al.* Mitigating errors on superconducting quantum processors through fuzzy clustering. *Advanced Quantum Technologies* **7**, 2300400 (2024).

[37] Magesan, E., Gambetta, J. M. & Emerson, J. Scalable and robust randomized benchmarking of quantum processes. *Phys. Rev. Lett.* **106**, 180504 (2011). URL <https://link.aps.org/doi/10.1103/PhysRevLett.106.180504>.

[38] Magesan, E. *et al.* Efficient measurement of quantum gate error by interleaved randomized benchmarking. *Phys. Rev. Lett.* **109**, 080505 (2012). URL <https://link.aps.org/doi/10.1103/PhysRevLett.109.080505>.

[39] Chen, J., Ding, D. & Huang, C. Randomized benchmarking beyond groups. *PRX Quantum* **3**, 030320 (2022). URL <https://link.aps.org/doi/10.1103/PRXQuantum.3.030320>.

[40] Cross, A. W., Magesan, E., Bishop, L. S., Smolin, J. A. & Gambetta, J. M. Scalable randomised benchmarking of non-Clifford gates. *npj Quantum Information* **2**, 16012 (2016).

[41] Helsen, J., Xue, X., Vandersypen, L. M. K. & Wehner, S. A new class of efficient randomized benchmarking protocols. *npj Quantum Information* **5**, 71 (2019).

[42] DiCarlo, L. *et al.* Demonstration of two-qubit algorithms with a superconducting quantum processor. *Nature* **460**, 240–244 (2009). URL <https://doi.org/10.1038/nature08121>.

[43] Krantz, P. *et al.* A quantum engineer’s guide to superconducting qubits. *Applied Physics Reviews* **6**, 021318 (2019).

[44] Negîrneac, V. *et al.* High-fidelity controlled- z gate with maximal intermediate leakage operating at the speed limit in a superconducting quantum processor. *Phys. Rev. Lett.* **126**, 220502 (2021). URL <https://link.aps.org/doi/10.1103/PhysRevLett.126.220502>.

[45] Koch, J. *et al.* Charge-insensitive qubit design derived from the cooper pair box. *Phys. Rev. A* **76**, 042319 (2007). URL <https://link.aps.org/doi/10.1103/PhysRevA.76.042319>.

[46] Zhao, P. *et al.* Quantum crosstalk analysis for simultaneous gate operations on superconducting qubits. *PRX Quantum* **3**, 020301 (2022). URL <https://link.aps.org/doi/10.1103/PRXQuantum.3.020301>.

[47] Ketterer, A. & Wellens, T. Characterizing crosstalk of superconducting transmon processors. *Phys. Rev. Appl.* **20**, 034065 (2023). URL <https://link.aps.org/doi/10.1103/PhysRevApplied.20.034065>.

[48] Cao, C. Non-trivial area operators require non-local magic. *Journal of High Energy Physics* **2024**, 105 (2024).

[49] Leone, L., Oliviero, S. F. E., Lloyd, S. & Hamma, A. Learning efficient decoders for quasi-chaotic quantum scramblers. *Physical Review A* **109**, 022429 (2024).

[50] Leone, L., Oliviero, S. F. E., Piemontese, S., True, S. & Hamma, A. Retrieving information from a black hole using quantum machine learning. *Physical Review A* **106**, 062434 (2022).

[51] Grier, D. & Schaeffer, L. The classification of Clifford gates over qubits. *Quantum* **6**, 734 (2022). URL <https://quantum-journal.org/papers/q-2022-06-13-734/>.

[52] Webb, Z. The Clifford group forms a unitary 3-design. *Quantum Information and Computation* **16**, 1379–1400 (2016).

[53] Stasino, V. *et al.* Implementation and readout of maximally entangled two-qubit gates quantum circuits in a superconducting quantum processor. *Journal of Superconductivity and Novel Magnetism* **38**, 129 (2025). URL <https://doi.org/10.1007/s10948-025-06968-x>.

[54] Bravyi, S., Sheldon, S., Kandala, A., Mckay, D. C. & Gambetta, J. M. Mitigating measurement errors in multiqubit experiments. *Physical Review A* **103**, 042605 (2021). URL <https://link.aps.org/doi/10.1103/PhysRevA.103.042605>.

[55] Kandala, A. *et al.* Error mitigation extends the computational reach of a noisy quantum processor. *Nature* **567**, 491–495 (2019). URL <https://doi.org/10.1038/s41586-019-1040-7>.

[56] Song, C. *et al.* Quantum computation with universal error mitigation on a superconducting quantum processor. *Science Advances* **5**, eaaw5686 (2019).

[57] Smith, A. W. R., Khosla, K. E., Self, C. N. & Kim, M. S. Qubit readout error mitigation with bit-flip averaging. *Science Advances* **7**, eabi8009 (2021).

[58] van den Berg, E., Minev, Z. K. & Temme, K. Model-free readout-error mitigation for quantum expectation values. *Phys. Rev. A* **105**, 032620 (2022). URL <https://link.aps.org/doi/10.1103/PhysRevA.105.032620>.

[59] Maciejewski, F. B., Zimborás, Z. & Oszmaniec, M. Mitigation of readout noise in near-term quantum devices by classical post-processing based on detector tomography. *Quantum* **4**, 257 (2020).

[60] Cosco, F., Plastina, F. & Lo Gullo, N. Bayesian mitigation of measurement errors in multiqubit experiments. *Physical Review A* **112**, 042621 (2025).

[61] Nielsen, M. A. & Chuang, I. L. *Quantum Computation and Quantum Information* (Cambridge University Press, Cambridge, UK, 2010). URL <https://books.google.it/books?id=-s4DEy7o-a0C>.

[62] Software package quantify. URL <https://quantify-os.org/>.

[63] Lucero, E. *et al.* High-fidelity gates in a single Josephson qubit. *Phys. Rev. Lett.* **100**, 247001 (2008). URL <https://link.aps.org/doi/10.1103/PhysRevLett.100.247001>.

[64] Reed, M. *Entanglement and Quantum Error Correction with Superconducting Qubits* (PhD Thesis). URL <https://books.google.it/books?id=7mORBQAAQBAJ>.

[65] Babu, A. P., Tuorila, J. & Ala-Nissila, T. State leakage during fast decay and control of a superconducting transmon qubit. *npj Quantum Information* **7**, 30 (2021). URL <https://doi.org/10.1038/s41534-020-00357-z>.

[66] Werninghaus, M. *et al.* Leakage reduction in fast superconducting qubit gates via optimal control. *npj Quantum Information* **7**, 14 (2021). URL <https://doi.org/10.1038/s41534-020-00346-2>.

[67] Motzoi, F., Gambetta, J. M., Rebentrost, P. & Wilhelm, F. K. Simple pulses for elimination of leakage in weakly nonlinear qubits. *Phys. Rev. Lett.* **103**, 110501 (2009). URL <https://link.aps.org/doi/10.1103/PhysRevLett.103.110501>.

[68] Rol, M. A. *et al.* Time-domain characterization and correction of on-chip distortion of control pulses in a quantum processor. *Applied Physics Letters* **116**, 054001 (2020).

[69] Rol, M. A. *et al.* Fast, high-fidelity conditional-phase gate exploiting leakage interference in weakly anharmonic superconducting qubits. *Phys. Rev. Lett.* **123**, 120502 (2019). URL <https://link.aps.org/doi/10.1103/PhysRevLett.123.120502>.

[70] Mallet, F. *et al.* Single-shot qubit readout in circuit quantum electrodynamics. *Nature Physics* **5**, 791–795 (2009). URL <https://doi.org/10.1038/nphys1400>.

[71] Gambetta, J. M. *et al.* Characterization of addressability by simultaneous randomized benchmarking. *Physical Review Letters* **109** (2012). URL <http://dx.doi.org/10.1103/PhysRevLett.109.240504>.

[72] Córcoles, A. D. *et al.* Process verification of two-qubit quantum gates by randomized benchmarking. *Phys. Rev. A* **87**, 030301 (2013). URL <https://link.aps.org/doi/10.1103/PhysRevA.87.030301>.

[73] Hashim, A. *et al.* Practical introduction to benchmarking and characterization of quantum computers. *PRX Quantum* **6**, 030202 (2025). URL <https://link.aps.org/doi/10.1103/PRXQuantum.6.030202>.

[74] Helsen, J., Roth, I., Onorati, E., Werner, A. & Eisert, J. General framework for randomized benchmarking. *PRX Quantum* **3**, 020357 (2022). URL <https://link.aps.org/doi/10.1103/PRXQuantum.3.020357>.

[75] Proctor, T. *et al.* Scalable randomized benchmarking of quantum computers using mirror circuits. *Phys. Rev. Lett.* **129**, 150502 (2022). URL <https://link.aps.org/doi/10.1103/PhysRevLett.129.150502>.

[76] Epstein, J. M., Cross, A. W., Magesan, E. & Gambetta, J. M. Investigating the limits of randomized benchmarking protocols. *Phys. Rev. A* **89**, 062321 (2014). URL <https://link.aps.org/doi/10.1103/PhysRevA.89.062321>.

[77] Wood, C. J. & Gambetta, J. M. Quantification and characterization of leakage errors. *Phys. Rev. A* **97**, 032306 (2018). URL <https://link.aps.org/doi/10.1103/PhysRevA.97.032306>.